

# Indoor Fluid Antenna Systems Enabled by Layout-Specific Modeling and Group Relative Policy Optimization

Tong Zhang, Qianren Li, Shuai Wang, *Senior Member, IEEE*, Wanli Ni, Jiliang Zhang, *Senior Member, IEEE*,  
Rui Wang, Kai-Kit Wong, *Fellow, IEEE*, and Chan-Byoung Chae, *Fellow, IEEE*

**Abstract**—The fluid antenna system (FAS) revolutionizes wireless communications by employing position-flexible antennas that dynamically optimize channel conditions and mitigate multipath fading. This innovation is particularly valuable in indoor environments, where signal propagation is severely degraded due to structural obstructions and complex multipath reflections. In this paper, we study the channel modeling and joint optimization of antenna positioning, beamforming, and power allocation for indoor FAS. In particular, we propose, for the first time, a layout-specific channel model and a novel group relative policy optimization (GRPO) algorithm for indoor FAS. Compared to the state-of-the-art Sionna model, our approach achieves an 83.3% reduction in computation time with an approximately 3 dB increase in root-mean-square error (RMSE). When simplified to a two-ray model, our channel model enables a closed-form solution for the optimal antenna position, achieving near-optimal performance. For the joint optimization problem, the proposed GRPO algorithm outperforms proximal policy optimization (PPO) and other baselines in sum-rate, while requiring only 49.2% computational resources of PPO, due to its group-based advantage estimation. Simulation results reveal that increasing either the group size or trajectory length in GRPO does not yield significant improvements in sum-rate, suggesting that these parameters can be selected conservatively without sacrificing performance.

**Index Terms**—Fluid antenna position optimization, beamforming, power allocation, group relative policy optimization.

## I. INTRODUCTION

MODERN wireless communications technologies have continuously transformed, with each generation marking a significant leap forward. The ongoing evolution from the fifth-generation (5G) to the sixth-generation (6G) represents

T. Zhang is with Guangdong Provincial Key Laboratory of Aerospace Communication and Networking Technology, Harbin Institute of Technology, Shenzhen, 518055, China (e-mail: tongzhang@hit.edu.cn).

Q. Li and R. Wang are with the Southern University of Science and Technology (e-mail: liqr2022@mail.sustech.edu.cn, wangr@sustech.edu.cn).

S. Zhang is with the Shenzhen Institute of Advanced Technology, Chinese Academy of Sciences, Shenzhen 518055, China (e-mail: s.wang@siat.ac.cn).

W. Ni is with the Department of Electronic Engineering, Tsinghua University, Beijing 100084, China (e-mail: niwanli@tsinghua.edu.cn).

J. Zhang is with the College of Information Science and Engineering, Northeastern University, Shenyang 110819, China (e-mail: zhangjiliang1@mail.neu.edu.cn).

K. K. Wong is with the Department of Electronic and Electrical Engineering, University College London, Torrington Place, U.K. He is also affiliated with the Yonsei Frontier Laboratory, Yonsei University, Seoul, 03722, South Korea (e-mail: kai-kit.wong@ucl.ac.uk).

C.-B. Chae is with the School of Integrated Technology, Yonsei University, Seoul 03722 South Korea (e-mail: cbchae@yonsei.ac.kr).

T. Zhang and Q. Li contributed equally.

Correspondence Authors: Jiliang Zhang and Shuai Wang.

Our GRPO code is available at [https://github.com/QianrenLi/rt\\_grpo](https://github.com/QianrenLi/rt_grpo).

a critical juncture in wireless communications development, characterized by groundbreaking technological shifts and innovative design approaches [1], [2], [3]. Despite numerous technological innovations, multiple-input multiple-output (MIMO) technique stands out as the most significant breakthrough in wireless communications of our time. One of MIMO's major innovations lies in its multiplexing gain, which allows simultaneous transmission of multiple data streams over the same frequency channel by leveraging multiple antennas [4]. Despite its prominent advantages, MIMO suffers from environment-dependent channel, which often leads to unstable performance if the number of antennas is not sufficient.

To mitigate this issue, fluid antenna system (FAS), a revolutionary advancement in antenna technology and wireless communications, was recently proposed in [5], [6], [7], [8]. It can be any software-controlled structures that can dynamically alter their physical configuration to optimize the radiating response according to the environments, which can be realized using a variety of reconfigurable antenna technologies such as [9], [10], [11], [12]. A key application of FAS is to circumvent deep fade or co-channel interference by changing the antenna position [13]. However, the current research on FAS primarily focuses on outdoor or unspecified scenarios [14], [15], [16], [17], in which channel modelling is statistical rather than site-specific. Such FAS statistical channel models include Rayleigh model [14], field response model [15], Jake's model [16], and Nakagami model [17]. But it was reported by Ericsson that 70% ~ 80% of mobile data traffic is generated indoors [18]. Unlike outdoor scenarios, indoor wireless is closely related to the environment, as its signal is easily blocked, reflected, and scattered by walls and other indoor objects [19]. Therefore, the fundamental challenges of FAS are on how to accurately model the indoor environment-aware channel and then configure FAS accordingly, which nevertheless remains unsolved.

Research on indoor wireless communications has been a thriving research area. For example, in [20], under statistical channel models, the authors illustrated that indoor wireless communication performance is significantly affected by wall blockages and derived analytical expressions for the average attenuation and for the signal-interference-ratio (SIR) performance. The authors of [21] proposed closed-form expressions to evaluate building wireless performance through two figures of merit, namely interference and power gains, analyzing how room dimensions impact wireless performance at different frequencies to provide guidance for wireless-friendly building

TABLE I: COMPARISON OF THIS WORK AND RELATED STUDIES ON FAS

Ref.	Site-Specific	Considered Scenario		Optimization Variables			Algorithmic Design		
		Single-User	Multi-User	FAS Position	Beamforming	Transmit Power	Numerical Methods	DRL	Closed-Form
[28]		✓		✓	✓	✓	✓		
[29]		✓	✓	✓	✓	✓	✓		
[30]		✓		✓		✓	✓		✓
[31]		✓	✓	✓	✓	✓	✓		
[32]		✓	✓	✓	✓	✓	✓		
[33]		✓	✓	✓	✓	✓	✓		
[34]		✓	✓	✓	✓	✓	✓		
[35]		✓	✓	✓	✓	✓		✓	
<b>Ours</b>	✓	✓	✓	✓	✓	✓		✓	✓

design. Aside from statistical channel modeling, a site-specific and accurate channel modeling approach, namely ray-tracing (RT), has been widely investigated for indoor wireless communications [22], [23], [24], [25], [26], [27].

The authors of [22] highlights that RT approach can provide accurate channel models for indoor wireless communications, and can be used for MIMO performance assessment, beamforming optimization, and real-time channel prediction. Then in [23], the authors examined how building materials affect indoor line-of-sight (LoS) MIMO wireless communications by developing a RT model that incorporates a wall reflection. Moreover, the authors of [24] developed a RT model for square layouts under single-reflection condition, considering both LoS and non-LoS (NLoS) rays to evaluate how building materials affect MIMO communications. Furthermore, it was found in [25] that LoS paths and wall-reflection paths dominate terahertz (THz) indoor channels through extensive measurements in a meeting room environment at 130-143 GHz.

Unlike traditional Fresnel's reflection model, [26] proposed an angle-independent constant reflection loss model for RT, which allows for a closed-form linear least squares solution when calibrating the ray tracer to real-world measurements. But real-world data is usually expensive to obtain. Sionna RT offers precise electromagnetic environment modeling with frequency-dependent material properties, and comprehensive propagation mechanisms including LoS paths, reflections, transmissions, and diffractions [27]. While Sionna offers high-fidelity simulation capabilities, its significant computational demands should not be underestimated, often necessitating GPU acceleration for efficient processing. To date, no indoor site-specific model for FAS that maintains a balance between high-fidelity and computational complexity, is available.

The optimization of FAS configurations has been extensively investigated in the literature. If discrete FAS positions, i.e., antenna port, a joint antenna port, beamforming, and transmit power optimization design for point-to-point MIMO communication was first investigated in [28], where rank-revealing QR decomposition, singular value decomposition (SVD), and water-filling have been used for antenna port, beamforming and transmit power optimization, respectively. Thereafter, the authors of [29] considered the downlink multi-user MISO FAS with discrete FAS positions, where graph theory was applied to address the antenna port optimization problem. Based on the derived outage probabilities, [30] optimized the throughput of the reconfigurable intelligent surface (RIS)-assisted FAS system.

Breaking the discrete FAS positions assumption, [31], [32]

studied downlink multi-user MISO FAS with continuous FAS positions, where the FASs are equipped at the transmitter [31] and receiver [32], respectively. Fractional-programming, zero-forcing (ZF), and successive convex approximation (SCA) algorithms have been designed for the joint antenna position, beamforming, and transmit power problem. Moreover, [33] and [34] tackled the maximization problem of the sensing signal-to-noise (SNR) with communication constraints for fluid antenna-assisted integrated sensing and communication (ISAC) systems by SCA and majorization-maximization (MM), respectively. Among optimization methods, deep reinforcement learning (DRL) is particularly powerful for solving complex decision-making problems with high-dimensional state and action spaces. In [35], an advantage actor-critic (A2C) DRL algorithm was applied to jointly optimize antenna position, beamforming, and transmit power in FAS for ISAC.

In this paper, we propose a layout-specific channel model, and a group relative policy optimization (GRPO) DRL solution for handling the coordinate optimization of antenna position, beamforming, and transmit power. A comparison of this work and related studies on FAS is given in Table I. Our contributions are summarized as follows:

- *Layout-Specific Model for FAS*: We propose a layout-specific channel model for the indoor FAS in a room. Specifically, given a layout, we introduce indicator functions for labeling NLoS and LoS rays, and design a low-complexity algorithm for computing the indicator function. After that, we model the fluid antenna position using polar coordinates, and analytically integrate the polar angles into the FAS channel model, leveraging the geometry. Unlike conventional MIMO systems, this approach provides a closed-form relationship between antenna movement and its impact on the channel model, enabling analytical analysis and concise optimization formulation for FAS. Moreover, a key advantage of our model is that it calculates wall reflections only once, significantly reducing computational complexity. Compared with the start-of-the-art Sionna model, simulation results show that our model achieves an 83.3% computational time reduction at the cost of approximately 3 dB root-mean-square-error (RMSE), highlighting the merit for practical use.
- *Closed-Form Solution for Two-Ray FAS Model*: We simplify our proposed layout-specific model to the two-ray model. Although the antenna position optimization for rate maximization is a non-convex problem, we derive a closed-form solution by exploiting the insights

TABLE II: DEFINITIONS OF SYMBOL NOTATION

Symbol	Definition	Symbol	Definition	Symbol	Definition
$N$	Number of transmit antennas	$K$	Number of receivers	$\theta_j$	Polar angle of transmit antenna $j$
$M$	Number of walls	$P_{\max}$	Maximal transmit power	$\theta_l$	Left boundary of FAS
$(x_1^c, y_1^c)$	Coordinate of corner point 1	$(x_0, y_0)$	Coordinate of Tx	$\theta_r$	Right boundary of FAS
$(x_1, y_1)$	Coordinate of Rx <sub>1</sub>	$\sigma^2$	Variance of AWGN	$\Delta$	Minimal $\theta$ between adjacent FAS antennas
$\alpha$	Angle of incidence	$S$	Reflection point on the wall	$d_{\text{LoS}}$	The length of LoS link
$d_{\text{NLoS}}$	The length of NLoS link	$\omega_1$	The beamforming vector for Rx <sub>1</sub>	$\mathbf{h}_1$	The channel vector from Tx to Rx <sub>1</sub>
$\pi$	MDP Policy	$\mathbf{s}$	MDP State	$\mathbf{a}$	MDP Action
$\mathbf{o}$	MDP observation	$r$	MDP reward	$O$	Trajectory length
$G$	Group size	$T$	Number of steps for PPO init.	$\epsilon_i$	Relative permittivity of wall $i$

in SNR function, namely the dominance and minimal length of the LoS path are important. Simulation results show that our closed-form solution delivers near-optimal performance across various problem settings, including rectangular layouts.

- *GRPO Solution for FAS*: For the joint optimization of antenna position, beamforming, and transmit power, we propose a GRPO solution that starts from a short-term trained proximal policy optimization (PPO) policy. Unlike PPO requires both A2C networks, GRPO optimizes memory utilization by leveraging group relative advantages, eliminating the need for the critic network. Extensive simulations show that our proposed GRPO solution achieves a higher sum-rate than PPO, advantage A2C, and fixed antenna position with weighted minimum mean-square-error (WMMSE). Our GRPO solution requires only 49.2% of the model size as well as floating-point operations per second (FLOPs) compared to PPO.

*Organization*: The system model and problem formulation are presented in Section II. Then Section III introduces the layout-specific RT model for FAS. A closed-form solution under a simplified single-wall reflection model is given in Section IV. GRPO solution for the joint optimization of antenna position, beamforming, and power allocation is proposed in Section V. Comprehensive simulation results are provided in Section VI. Conclusions are drawn in Section VII.

*Notation*:  $(\cdot)^*$  denotes conjugate operation.  $\mathbb{E}\{\cdot\}$  denotes the long-term expectation operator.  $\mathcal{O}(\cdot)$  denotes that for real functions  $f(x), g(x)$  from  $\mathbb{R}$  to  $\mathbb{R}$ ,  $f(x) = \mathcal{O}(g(x))$  means  $\limsup_{x \rightarrow \infty} \frac{|f(x)|}{|g(x)|} < \infty$ . Also,  $[A]$  is a set containing elements from 1 to  $A$ , and  $\|\cdot\|_2$  is Euclidean norm. The notation  $\lfloor x \rfloor$  represents the floor of  $x$ ,  $\lceil x \rceil$  represents the ceiling of  $x$ , and  $\text{round}(x)$  represents rounding  $x$  to the nearest integer. Some notation definitions are given in Table II.

## II. SYSTEM MODEL AND PROBLEM FORMULATION

We consider a FAS deployed in a room, where all the walls are assumed to be either perpendicular or parallel. We also consider there are  $K$  receivers, denoted by Rx, and a single transmitter, denoted by Tx, within this layout, where each Rx has a single antenna, while Tx has  $N$  fluid antennas and  $K \leq N$ . Tx aims to communicate with all Rxs simultaneously, thus creating undesired interference to each Rx. The additive white Gaussian noise (AWGN) is expressed as  $\mathcal{CN}(0, \sigma^2)$ .

Specifically, there exists a room layout with  $M$  walls, for radio propagation, there exist multiple rays from Tx to Rx. An example of room layout is as shown in Fig. 1. A

square coordinate system with  $x$ -axis and  $y$ -axis is introduced. The locations of Rx <sub>$k$</sub> ,  $k \in [K]$ , and Tx are denoted by  $(x_k, y_k)$ ,  $k \in [K]$ , and  $(x_0, y_0)$ , respectively, represented as a set  $\mathcal{X} \triangleq \{x_0, y_0, x_1, y_1, \dots, x_K, y_K\}$ . We assume a rectilinear layout, where all walls are either perpendicular or parallel to the  $x$ -axis. This configuration is widely recognized as a preliminary and predominant layout in the design of rectangular architectural layouts [36]. Conveniently, we describe this layout by specifying the corner points of each wall. The corner points in clockwise order are denoted by  $(0, 0), (x_1^c, y_1^c), \dots, (x_{M-1}^c, 0)$ , respectively, and represented as a set  $\mathcal{L} \triangleq \{0, 0, x_1^c, y_1^c, \dots, x_{M-1}^c, 0\}$ . Given room layout  $\mathcal{L}$  and Tx-Rx locations  $\mathcal{X}$ , the channel from Tx to Rx  $k$  is parameterized by polar angle  $\theta_j$ ,  $j \in [N]$  of antenna  $j$ 's position, denoted by  $\mathbf{h}_k(\boldsymbol{\theta})$ , where  $\boldsymbol{\theta} = (\theta_1, \dots, \theta_N)$ . Tx transmits one data stream to each Rx with beamforming vector  $\omega_k$ . The signal-to-interference-noise ration (SINR) at Rx  $k$  is expressed as  $\frac{|\mathbf{h}_k^H(\boldsymbol{\theta})\omega_k|^2}{\sum_{k' \neq k} |\mathbf{h}_{k'}^H(\boldsymbol{\theta})\omega_k|^2 + \sigma^2}$ , and the data rate at Rx  $k$  is expressed as  $\log_2(1 + \frac{|\mathbf{h}_k^H(\boldsymbol{\theta})\omega_k|^2}{\sum_{k' \neq k} |\mathbf{h}_{k'}^H(\boldsymbol{\theta})\omega_k|^2 + \sigma^2})$ . Our objective is to maximize the sum-rate through joint optimization of the fluid antenna positions, power allocation, and beamforming vectors. This optimization problem is formulated as follows:

$$\begin{aligned}
 \text{(P1)} \quad & \max_{\boldsymbol{\theta}, \{\omega_k\}} \sum_{k=1}^K \log_2 \left( 1 + \frac{|\mathbf{h}_k^H(\boldsymbol{\theta})\omega_k|^2}{\sum_{k' \neq k} |\mathbf{h}_{k'}^H(\boldsymbol{\theta})\omega_k|^2 + \sigma^2} \right) \\
 \text{s.t.} \quad & \sum_{k=1}^K \|\omega_k\|_2^2 \leq P_{\max}, \quad (1a) \\
 & \theta_l \leq \theta_1 \leq \theta_2 \leq \dots \leq \theta_K \leq \theta_r, \quad (1b) \\
 & \Delta \leq |\theta_{k'} - \theta_{k''}|, \quad \forall k', k'' \in [K], \quad (1c)
 \end{aligned}$$

where constraint (1a) ensures the total transmission power remains within the allowable limit  $P_{\max}$ , constraint (1b) guarantees that the optimized FAS antenna positions are sequentially ordered, and constraint (1c) enforces a minimum separation  $\Delta$  between adjacent FAS antennas to avoid mutual coupling.

Prior to solving Problem (P1), we shall establish the model of  $\mathbf{h}_k(\boldsymbol{\theta})$ . This model should satisfy two key requirements: 1) the ability to capture the multi-rays propagating in a room layout; 2) the channel should depend uniquely on the parameters  $\theta_j$ ,  $j \in [N]$ . In the next section, we propose a model that fulfills the aforementioned requirements.

## III. PROPOSED LAYOUT-SPECIFIC RT MODEL FOR FAS

To model the layout-specific RT channel, we consider the ray reflection on each wall only once. After determining

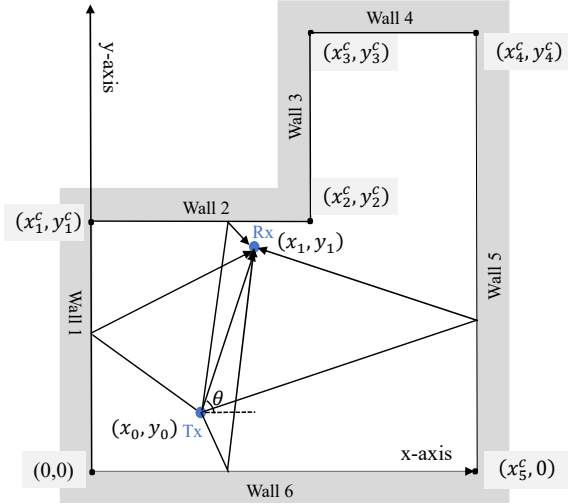


Fig. 1: A room layout for exemplified illustration.

whether there is a ray reflection on each wall, we analytically express the length of NLoS and LoS rays. Given a room layout  $\mathcal{L}$  and Tx-Rxs locations  $\mathcal{X}$ , we model this layout specific RT channel as  $\mathbf{h}_k(\mathcal{L}, \mathcal{X}) = (h_{k,1}(\mathcal{L}, \mathcal{X}), \dots, h_{k,N}(\mathcal{L}, \mathcal{X}))$ , where  $h_{k,j}(\mathcal{L}, \mathcal{X})$ ,  $j \in [N]$  denotes the per-antenna channel from Tx-antenna  $j$  to Rx  $k$  and is modeled in (2), shown on the top of next page, where  $\lambda$  denotes the wavelength,  $\epsilon_i$  denotes the relative permittivity of wall  $i$ ,  $\alpha_{i,k,j}$  denotes the angle of incidence on wall  $i$  for Rx $_k$ 's NLoS ray  $j$ ,  $\Gamma_{i,k,j}$  denotes the reflection loss on wall  $i$  for Rx $_k$ 's NLoS ray  $j$ . The wavelength  $\lambda$  is calculated by  $3 \times 10^8 / f$ , where  $f$  denotes the frequency. Specifically, we introduce indicator functions in (2) to indicate the absence or presence of rays.

The indicator function is represented by  $\mathbb{1}_{\text{Wall-}i,k,j}(\mathcal{L}, \mathcal{X})$  for  $i \in [M]$ ,  $k \in [K]$ ,  $j \in [N]$ , where 1 indicates the existence of an NLoS ray of wall  $i$ , and 0 indicates its absence. Similarly, we define  $\mathbb{1}_{\text{LoS},j}(\mathcal{L}, \mathcal{X})$ ,  $j \in [N]$ . Given a room layout, all indicator functions can be determined by means of Algorithm 1. The computational complexity of Algorithm 1 can be assessed across its three steps, with  $M$  walls in the set  $\mathcal{L}$  and a fixed Tx-Rx pair in  $\mathcal{X}$ . Step 1 checks each wall in  $\mathcal{O}(M)$ . Step 2 computes reflection points for up to  $M$  walls, also taking  $\mathcal{O}(M)$ . Step 3, the most demanding, involves checking each of the up to  $M$  filtered walls against all  $M$  walls for blockages, resulting in  $\mathcal{O}(M^2)$ . Step 4 checks the LoS against all  $M$  walls in  $\mathcal{O}(M)$ . Since Step 3 dominates, the overall computational complexity of Algorithm 1 is  $\mathcal{O}(M^2)$ .

Once the indicator functions are decided, we need to parameterize the length of NLoS ray  $d_{\text{NLoS-}i,k,j}$ , and the length of LoS ray  $d_{\text{LoS},j}$ , and Fresnel's reflection coefficient  $\Gamma_{i,k,j}$  with antenna  $j$ 's polar angle  $\theta_j$ . This is accomplished by introducing angle-dependent distance functions  $D_{i,k}^{[1]}(\theta_j)$ ,  $D_{i,k}^{[2]}(\theta_j)$  and  $D_{i,k}^{[3]}(\theta_j)$ , where  $D_{i,k}^{[1]}(\theta_j)$  and  $D_{i,k}^{[2]}(\theta_j)$  denote the perpendicular Euclidean distances from Tx and Rx to wall  $i$ , respectively, and  $D_{i,k}^{[3]}(\theta_j)$  denotes the horizontal Euclidean distance between Tx and Rx.

We now demonstrate the parameterization of the terms  $d_{\text{NLoS-}i,k,j}$ ,  $d_{\text{LoS},j}$ , and  $\Gamma_{i,k,j}$  with respect to the angle  $\theta_j$ .

---

### Algorithm 1: Indicator Functions Computation

---

**Input:** Tx-Rx set  $\mathcal{X}$ , Wall set  $\mathcal{L}$

- 1 Set 1 to  $\{\mathbb{1}_{\text{Wall-}i,k,j}(\mathcal{L}, \mathcal{X})\}$ , and to  $\mathbb{1}_{\text{LoS},j}(\mathcal{L}, \mathcal{X})$ .
- 2 **Step 1: Compute Reflection Points**  $\{S_i\}$  in  $\mathcal{L}$
- 3 **for each Wall**  $i$  **in**  $\mathcal{L}$  **do**
- 4     **if wall**  $i$  **is perpendicular to y-axis then**
- 5         Compute (5) for  $u$ .  $S_i = (x_0 + u, y_i^c)$ .
- 6     **end**
- 7     **if wall**  $i$  **is perpendicular to x-axis then**
- 8         Compute (5) for  $u$ .  $S_i = (x_i^c, y_0 + u)$ .
- 9     **end**
- 10 **end**
- 11 **Step 2: Identify Blockage in**  $\mathcal{L}$
- 12 **for each Wall**  $i$  **in**  $\mathcal{L}$  **do**
- 13     Line equation  $\ell_i^{[1]}$  generation by  $(x_0, y_0)$  and  $S_i$ .
- 14     Line equation  $\ell_i^{[2]}$  generation by  $(x_1, y_1)$  and  $S_i$ .
- 15     **for each wall**  $i'$  **in**  $\mathcal{L}$  **do**
- 16         **if The linear system**  $\ell_i^{[1]}$ ,  $x = x_{i'}^c - x_{i'-1}^c$ , and  $y = y_{i'}^c - y_{i'-1}^c$  **has a non-zero solution then**
- 17              $\mathbb{1}_{\text{Wall-}i,k,j}(\mathcal{L}, \mathcal{X}) = 0$ .
- 18         **end**
- 19         **if The linear system**  $\ell_i^{[2]}$ ,  $x = x_{i'}^c - x_{i'-1}^c$ , and  $y = y_{i'}^c - y_{i'-1}^c$  **has a non-zero solution then**
- 20              $\mathbb{1}_{\text{Wall-}i,k,j}(\mathcal{L}, \mathcal{X}) = 0$ .
- 21         **end**
- 22     **end**
- 23 **Step 3: Identify Blockage in LoS Ray**
- 24     Line equation  $\ell_i^{[3]}$  generation by  $(x_0, y_0)$  and  $(x_1, y_1)$ .
- 25     **for each wall**  $i'$  **in**  $\mathcal{L}$  **do**
- 26         **if The linear system**  $\ell_i^{[3]}$ ,  $x = x_{i'}^c - x_{i'-1}^c$ , and  $y = y_{i'}^c - y_{i'-1}^c$  **has a non-zero solution then**
- 27              $\mathbb{1}_{\text{LoS},j}(\mathcal{L}, \mathcal{X}) = 0$ .
- 28     **end**

**Output:**  $\{\mathbb{1}_{\text{Wall-}i,k,j}(\mathcal{L}, \mathcal{X})\}$ ,  $\mathbb{1}_{\text{LoS},j}(\mathcal{L}, \mathcal{X})$

---

For notational simplicity, the subscripts are omitted in the subsequent analysis. As revealed by the geometry in Fig. 2, the following equation holds,

$$\tan \alpha = \frac{D^{[1]}(\theta)}{u}, \quad (4a)$$

$$\tan \alpha = \frac{D^{[2]}(\theta)}{D^{[3]}(\theta) - u}, \quad (4b)$$

where  $u$  can be solved from (4a) and (4b) as

$$u = \frac{D^{[1]}(\theta)D^{[3]}(\theta)}{D^{[1]}(\theta) + D^{[2]}(\theta)}. \quad (5)$$

Next, we eliminate  $u$  in (4a)-(4b) and obtain,

$$\tan \alpha = \frac{D^{[1]}(\theta) + D^{[2]}(\theta)}{D^{[3]}(\theta)}. \quad (6)$$

The length of NLoS ray obeys the following relationship,

$$(d_1 + d_2) \sin \alpha = D^{[1]}(\theta) + D^{[2]}(\theta), \quad (7)$$

$$h_{k,j}(\mathcal{L}, \mathcal{X}) = \frac{\sqrt{G_t G_r} \lambda}{4\pi} \left( \underbrace{\sum_{i=1}^M \mathbb{1}_{\text{Wall-}i,k,j}(\mathcal{L}, \mathcal{X}) \frac{\Gamma_{i,k,j} \exp(-j2\pi \frac{d_{\text{NLoS-}i,k,j}}{\lambda})}{d_{\text{NLoS-}i,k,j}}}_{\text{NLoS Ray}} + \underbrace{\mathbb{1}_{\text{LoS},j}(\mathcal{L}, \mathcal{X}) \frac{\exp(-j2\pi \frac{d_{\text{LoS},j}}{\lambda})}{d_{\text{LoS},j}}}_{\text{LoS Ray}} \right), \quad (2)$$

where

$$\Gamma_{i,k,j} = \begin{cases} \frac{-\epsilon_i \sin \alpha_{i,k,j} + \sqrt{\epsilon_i - \cos^2 \alpha_{i,k,j}}}{\epsilon_i \sin \alpha_{i,k,j} + \sqrt{\epsilon_i - \cos^2 \alpha_{i,k,j}}}, & \text{Transverse Magnetic (TM) Mode,} \\ \frac{\sin \alpha_{i,k,j} - \sqrt{\epsilon_i - \cos^2 \alpha_{i,k,j}}}{\sin \alpha_{i,k,j} + \sqrt{\epsilon_i - \cos^2 \alpha_{i,k,j}}}, & \text{Transverse Electric (TE) Mode.} \end{cases} \quad (3)$$

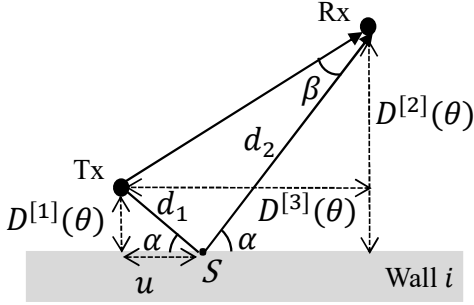


Fig. 2: The two-ray model under reflection of wall  $i$ .

Since  $\sin \alpha = \frac{\tan \alpha}{\sqrt{1+\tan^2 \alpha}}$ , (6), and (7), we arrive at

$$d_{\text{NLoS}} = d_1 + d_2 = \sqrt{D^{[3]^2}(\theta) + (D^{[1]}(\theta) + D^{[2]}(\theta))^2}, \quad (8)$$

Furthermore, we express Fresnel's reflection coefficient  $\Gamma$  with  $D^{[1]}(\theta)$ ,  $D^{[2]}(\theta)$  and  $D^{[3]}(\theta)$ .

For arbitrary wall  $i$  in layout  $\mathcal{L}$ , we can obtain its  $\alpha$  and  $d_{\text{NLoS}}$  by (6) and (8), respectively. Finally, it can be seen that

$$d_{\text{LoS}} = \begin{cases} \frac{y_1 - y_0}{\sin \theta}, & \theta \in (\arctan \frac{y_1 - y_0}{x_1}, \frac{\pi}{2}), \\ \frac{y_1 - y_0}{\sin(\pi - \theta)} = \frac{y_1 - y_0}{\sin \theta}, & \theta \in [\frac{\pi}{2}, \pi - \arctan \frac{y_1 - y_0}{x_1}]. \end{cases} \quad (9)$$

As a final step, we shall derive the angle-dependent distances  $D^{[1]}(\theta)$ ,  $D^{[2]}(\theta)$ , and  $D^{[3]}(\theta)$  for a given room layout. This derivation is achieved by expressing these distances in terms of a unified coordinate representation, where the distance variables are parameterized by the polar angle  $\theta$ . Please refer to Appendix A for an example. Through  $D^{[1]}(\theta)$ ,  $D^{[2]}(\theta)$ ,  $D^{[3]}(\theta)$ , and Algorithm 1,  $h_{k,j}(\theta)$  can be obtained via (2) and (3), thereby yielding the desired expression for  $\mathbf{h}_k(\theta)$ .

#### A. Discussion on Spatial Correlation

Moreover, we discuss the spatial correlation for the proposed channel model as follows. Unlike statistical FAS channel models in [16], [37], [38], we model the spatial correlation in deterministic propagation environments by the RT method. Therefore, the spatial correlation is inherently characterized by the ray propagation [39]. According to [39], the correlation between the channel from transmit antenna  $j_1$  to  $\text{Rx}_k$ , i.e.,

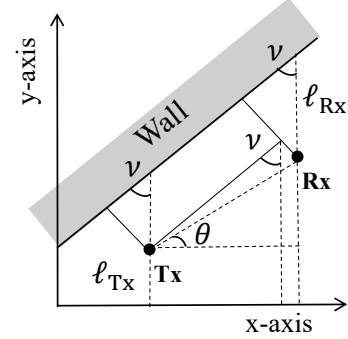


Fig. 3: Illustration of the angle-dependent distance derivation for an oblique wall.

$h_{k,j_1}(\theta)$  and the channel from transmit antenna  $j_2$  to  $\text{Rx}_k$ , i.e.,  $h_{k,j_2}(\theta)$  can be calculated by

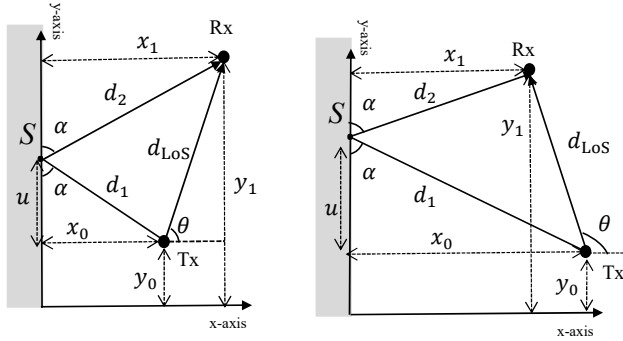
$$\rho_{1,2} = \frac{h_{k,j_1}(\theta) h_{k,j_2}^*(\theta)}{|h_{k,j_1}(\theta)|^2 |h_{k,j_2}(\theta)|^2}, \quad (10)$$

where  $0 \leq |\rho_{1,2}| \leq 1$ ,  $|\rho_{1,2}| = 1$  represents a linear correlation and  $|\rho_{1,2}| = 0$  represents no correlation.

#### B. Discussion on Arbitrary Geometry Layout

In the presence of oblique walls, shown in Fig. 3, the changes lie in deriving the angle-dependent distances  $D^{[1]}(\theta)$ ,  $D^{[2]}(\theta)$ , and  $D^{[3]}(\theta)$  as well as indicator function computation algorithm, such that  $\mathbf{h}_k(\theta)$  can be obtained via (2) and (3). The complexity arises from the wall's slope, which introduces nontrivial geometric and dependencies into both the distance functions and the indicator function computation. Specifically, for the angle-dependent distance derivation, we shall first derive the intersection points of the upward prolongation lines  $l_{\text{Tx}}$ ,  $l_{\text{Rx}}$ , and the wall. After that, we can have the distance between the intersection point and Tx or Rx. Finally, since slope angle  $\nu$  is known,  $D^{[1]}(\theta)$  and  $D^{[2]}(\theta)$  can be derived. Since the distance between Tx and Rx can be obtained by  $d_{\text{LoS}}$ ,  $D^{[3]}(\theta)$  can be derived as  $d_{\text{LoS}} \cos(\frac{\pi}{2} - \theta - \nu)$ . For the indicator function computation, the wall's slope must be considered when computing reflection points. To properly detect blockages, the oblique wall equation replaces the corresponding perpendicular or parallel to  $x$ -axis equation.

In the presence of curved walls, this scenario becomes significantly more complex. The RT algorithm proposed in

(a) When  $\arctan \frac{y_1 - y_0}{x_1} \leq \theta < \frac{\pi}{2}$ (b) When  $\frac{\pi}{2} \leq \theta < \pi$ Fig. 4: Two-ray model (single-wall reflection only), where the reflection point on the wall is denoted by  $S$ .

Sionna [27] should be employed, where both reflection point computation and blockage identification are handled algorithmically rather than through semi-closed-form expressions.

#### IV. CLOSED-FROM SOLUTION FOR TWO-RAY MODEL

It can be seen that Problem (P1) poses a significant challenge due to its non-convex nature, stemming from the channel model in the objective function. To show this issue edgewise, we show the landscape of  $\|\mathbf{h}_1(\theta)\|_2$  and  $\|\mathbf{h}_2(\theta)\|_2$  in Fig. 5 for the rectangular layout and Fig. 1 layout with  $N = 2$  and  $K = 2$ . As illustrated in Fig. 5, the landscape reveals a multitude of local optima, which complicates the application of conventional numerical optimization techniques and hinders their ability to achieve a high-performing solution. Therefore, in this section, we first simplify the channel model from the layout-specific downlink multi-user MISO to the single-wall reflection with single-antenna point-to-point transmission, i.e., two-ray. By this way, we can have a reduced form of Problem (P1) and next obtain a closed-form solution by leveraging some key insights.

If we assume that there are only one Rx with a single antenna at Tx. Furthermore, we assume that there exists only a wall rather than a layout for simplicity. As shown in Fig. 4, we have one Rx, whose location is denoted by  $(x_1, y_1)$ . The wall is perpendicular to  $x$ -axis. The channel is given by

$$h_2(\mathcal{L}, \mathcal{X}) = \frac{\sqrt{G_t G_r} \lambda}{4\pi} \left( \underbrace{\frac{\Gamma \exp(-j2\pi \frac{d_{\text{NLoS}}}{\lambda})}{d_{\text{NLoS}-i,k,j}}}_{\text{NLoS Ray}} + \underbrace{\frac{\exp(-j2\pi \frac{d_{\text{LoS}}}{\lambda})}{d_{\text{LoS}}}}_{\text{LoS Ray}} \right), \quad (12)$$

where  $\Gamma$  is from (3). The key to express the channel with  $\theta$  is writing down  $D^{[1]}(\theta)$ ,  $D^{[2]}(\theta)$ , and  $D^{[3]}(\theta)$ . After that, we are able to arrive at  $h_2(\theta)$  using (6), (8), and (9). Finally,  $\text{SNR}_2(\theta) = |h_2(\theta)|^2 / \sigma^2$ . The expression of  $\text{SNR}_2(\theta)$  is given by below Theorem.

**Theorem 1.** Given the simplified single-wall reflection model with point-to-point transmission, SNR function is given in (11),

shown on the top of next page, where  $\theta \in (\arctan \frac{y_1 - y_0}{x_1}, \pi)$  and  $\Gamma$  is from substituting  $\alpha = \arctan(\frac{2x_1}{y_1 - y_0} - \frac{1}{\tan \theta})$  into (3).

*Proof:* Please refer to Appendix B. ■

It can be observed from (11) that there are three terms in  $\text{SNR}_2(\theta)$ : the first term is exclusively influenced by the NLoS ray, the second term is solely affected by the LoS ray, and the third term represents the interaction/interference between NLoS and LoS rays. For this simplified problem, Problem (P1) reduces to,

$$(P2) \quad \max_{\theta} \quad \log_2(1 + \text{SNR}_2(\theta)) \quad (13a)$$

$$\text{s.t.} \quad \theta_l \leq \theta \leq \theta_r, \quad (13b)$$

where  $\theta$  can be varied from the lower bound  $\theta_l$  to the upper bound  $\theta_r$ . In an interference-free scenario, maximizing  $\log_2(1 + \text{SNR}_2(\theta))$  is equivalent to maximizing  $\text{SNR}_2(\theta)$ .

Despite depending on a single variable,  $\text{SNR}_2(\theta)$  defies a closed-form solution due to its complex structure. The parameter  $\theta$  appears within trigonometric functions in both numerator and denominator terms, making analytical simplification extraordinarily difficult. When applying numerical optimization methods like gradient descent, initial point selection becomes critical. As illustrated in Fig. 6, the highly oscillatory and irregular landscape of  $\text{SNR}_2(\theta)$  hinders the identification of initial points that consistently converge to satisfactory local optima. Nevertheless, through rigorous examination of  $\text{SNR}_2(\theta)$ 's properties, we derive key insights enabling the development of a low-complexity closed-form solution.

To address Problem (P1) and obtain a closed-form solution, the properties of the function  $\text{SNR}_2(\theta)$  play a critical role. To elucidate these properties by examples, we analyze a specialized case depicted in Fig. 6. Two significant observations arise from Fig. 6: 1) *LoS term within  $\text{SNR}_2(\theta)$  predominantly governs the function, with NLoS term contributing only marginally;* 2) *the superposition of the LoS and NLoS terms yields a unimodal function, attaining its maximum at  $\theta = \pi/2$  when this value is feasible. Moreover, the rate function exhibits oscillatory behavior synchronized with the frequency of the cosine term in the NLoS-LoS interaction component.* These findings provide the insights for devising a closed-form solution.

The proposed closed-form solution to Problem (P2), denoted as  $\theta^*$ , is systematically categorized into three cases, each expounded below on a case-by-case basis.

**Case 1** When  $\theta_l, \theta_r \in (\arctan \frac{y_1 - y_0}{x_1}, \frac{\pi}{2})$  and  $\theta_l \leq \theta_r$ , the solution lies the leftmost local maximizer to  $\theta_r$  or  $\theta_r$  itself. It can be seen that the oscillation comes from the cos function in the NLoS-LoS interaction term; and  $(\sqrt{(y_1 - y_0)^2 + (2x_1 - \frac{y_1 - y_0}{\tan \theta})^2} - \frac{y_1 - y_0}{\sin \theta}) / \lambda$  is monotonically increasing in  $\theta$  if  $\theta \in [\arctan \frac{y_1 - y_0}{2x_1}, \pi)$ . Through trigonometric identities and algebra manipulation, the closed-form solution  $\theta^*$  is given in below proposition.

**Proposition 1.** When  $\theta_l, \theta_r \in (\arctan \frac{y_1 - y_0}{x_1}, \frac{\pi}{2})$  and  $\theta_l \leq \theta_r$ , the closed-form solution  $\theta^*$  to Problem (P2) is given by

$$\theta^* = \arg \max \{ \text{SNR}_2(f(n)), \text{SNR}_2(\theta_r) \}, \quad (14)$$

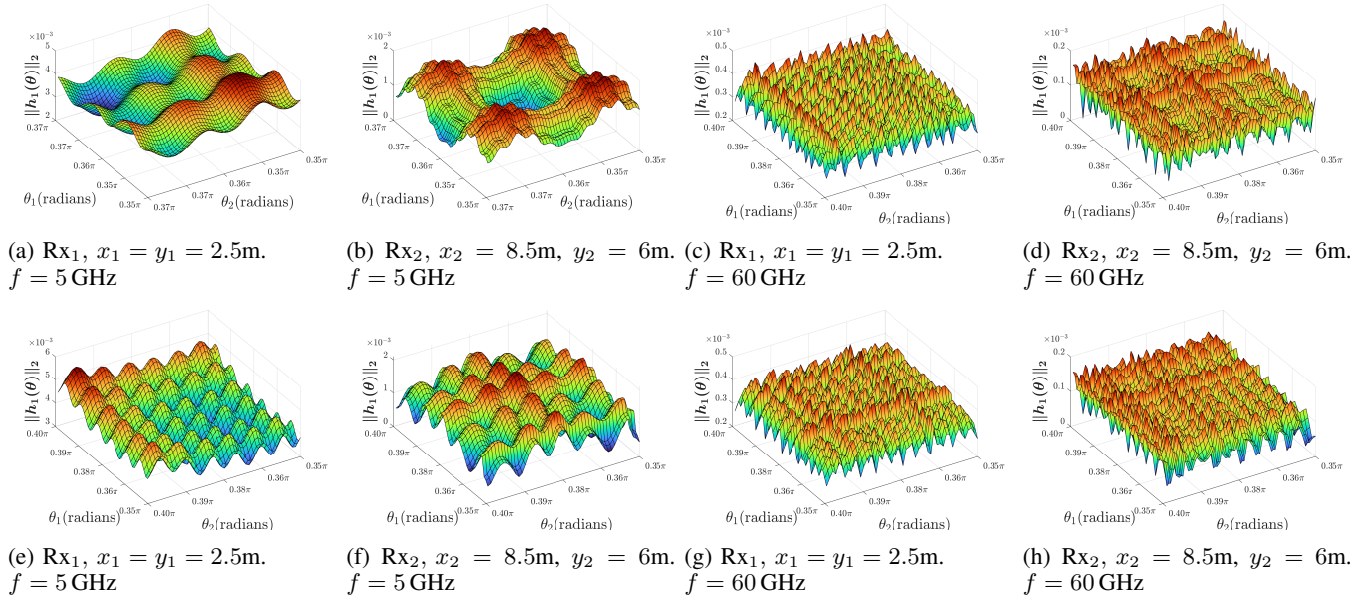


Fig. 5: Landscape of  $\|\mathbf{h}_k(\boldsymbol{\theta})\|_2$ ,  $k = 1, 2$ , in TE mode,  $G_t = G_r = 1$ ,  $\sigma^2 = -90$  dBm,  $y_0 = 1$  m,  $f = 5$  GHz,  $\epsilon = 5.24$ . Subfigures (a)–(d): Rectangular layout with corner points  $\{(0, 0), (0, 10), (10, 10), (10, 0)\}$  (Unit: m). Subfigures (e)–(g): Irregular layout following Fig. 1, with corner points  $\{(0, 0), (0, 5), (5, 8), (8, 8), (8, 10), (10, 10), (10, 0)\}$  (Unit: m).

$$\text{SNR}_2(\theta) = \frac{G_t G_r \lambda^2}{\sigma^2 (4\pi)^2} \left( \underbrace{\frac{\Gamma^2}{(y_1 - y_0)^2 + (2x_1 - \frac{y_1 - y_0}{\tan \theta})^2}}_{\text{NLoS Term}} + \underbrace{\frac{\sin^2 \theta}{(y_1 - y_0)^2}}_{\text{LoS Term}} + \underbrace{\frac{2\Gamma \cos \left( 2\pi \frac{\sqrt{(y_1 - y_0)^2 + (2x_1 - \frac{y_1 - y_0}{\tan \theta})^2} - \frac{y_1 - y_0}{\sin \theta}}{\lambda} \right)}{\frac{y_1 - y_0}{\sin \theta} \sqrt{(y_1 - y_0)^2 + (2x_1 - \frac{y_1 - y_0}{\tan \theta})^2}}}_{\text{NLoS-LoS Interaction Term}} \right), \quad (11)$$

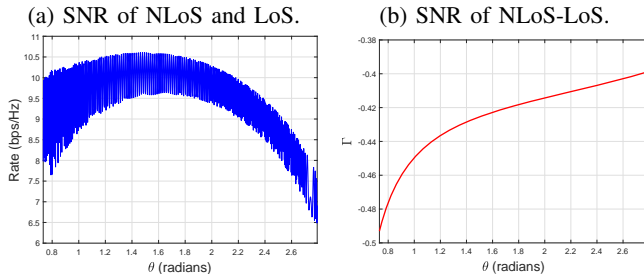
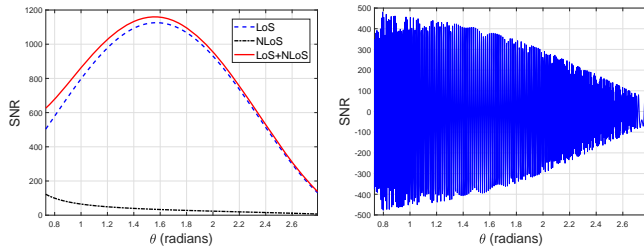


Fig. 6: TE mode,  $G_t = G_r = 1$ ,  $\sigma^2 = -90$  dBm,  $x_1 = y_1 = 5$  m,  $x_0 = 0.5$  m,  $f = 5$  GHz,  $\epsilon = 5.24$ .

where if  $\Gamma \neq 0$ , then

$$f(n) = \arcsin \left( \frac{n\lambda(y_1 - y_0)}{\sqrt{(4x_1^2 - \frac{n^2\lambda^2}{4})^2 + (4x_1(y_1 - y_0))^2}} \right)$$

$$- \arctan \left( \frac{-4x_1(y_1 - y_0)}{4x_1^2 - \frac{n^2\lambda^2}{4}} \right), \quad (15)$$

and

$$n = \begin{cases} 2 \lfloor \frac{\sqrt{(y_1 - y_0)^2 + (2x_1 - \frac{y_1 - y_0}{\tan \theta_r})^2} - \frac{y_1 - y_0}{\sin \theta_r}}{\lambda} \rfloor, & 0 < \Gamma, \\ 2 \lfloor \frac{\sqrt{(y_1 - y_0)^2 + (2x_1 - \frac{y_1 - y_0}{\tan \theta_r})^2} - \frac{y_1 - y_0}{\sin \theta_r}}{\lambda} \rfloor - 1, & \Gamma < 0. \end{cases} \quad (16)$$

*Proof:* Please refer to Appendix C. ■

**Case 2** When  $\theta_l \in (\arctan \frac{y_1 - y_0}{x_1}, \frac{\pi}{2})$  and  $\theta_r \in [\frac{\pi}{2}, \pi - \arctan \frac{y_1 - y_0}{x_1})$ , the solution lies the closest local maximizer to  $\frac{\pi}{2}$  or  $\frac{\pi}{2}$  itself. The closed-form solution  $\theta^*$  to Problem (P2) is given by

$$\theta^* = \arg \max \{ \text{SNR}_2(f(n_1)), \text{SNR}_2(f(n_2)), \text{SNR}_2(\pi/2) \}, \quad (17)$$

where if  $\Gamma \neq 0$ , then  $f(n_1)$  and  $f(n_2)$  exist with

$$n_1 = \begin{cases} 2 \lfloor \frac{\sqrt{(y_1 - y_0)^2 + 4x_1^2 - (y_1 - y_0)}}{\lambda} \rfloor, & 0 < \Gamma, \\ 2 \lfloor \frac{\sqrt{(y_1 - y_0)^2 + 4x_1^2 - (y_1 - y_0)}}{\lambda} \rfloor - 1, & \Gamma < 0, \end{cases} \quad (18)$$

and

$$n_2 = \begin{cases} 2 \lfloor \frac{\sqrt{(y_1 - y_0)^2 + 4x_1^2 - (y_1 - y_0)}}{\lambda} \rfloor, & 0 < \Gamma, \\ 2 \lfloor \frac{\sqrt{(y_1 - y_0)^2 + 4x_1^2 - (y_1 - y_0)}}{\lambda} \rfloor + 1, & \Gamma < 0. \end{cases} \quad (19)$$

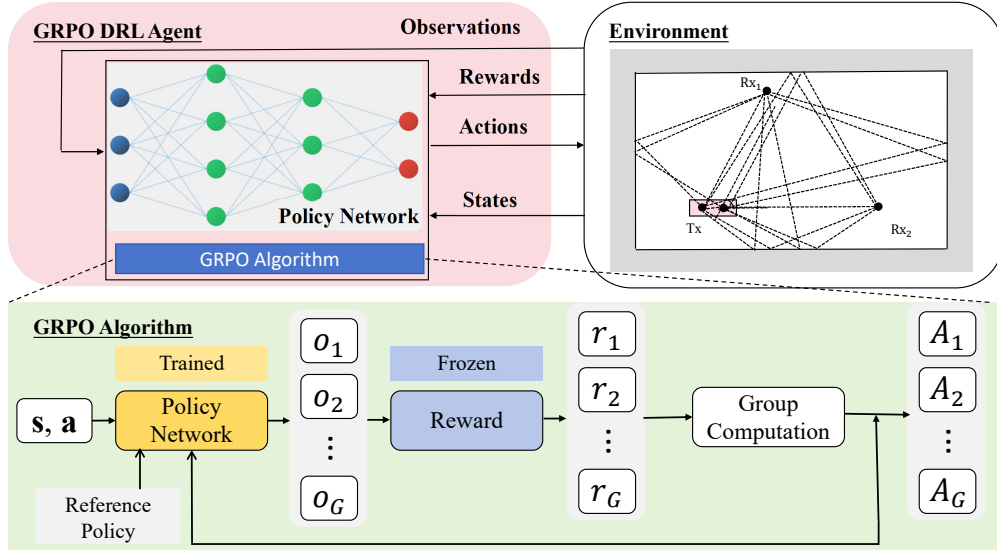


Fig. 7: Illustration of the algorithm framework of GRPO training.

**Case 3** When  $\theta_l, \theta_r \in [\frac{\pi}{2}, \pi - \arctan \frac{y_1 - y_0}{x_1}]$  and  $\theta_l \leq \theta_r$ , the solution lies the rightmost local maximizer to  $\theta_l$  or  $\theta_l$  itself. The closed-form solution  $\theta^*$  to Problem (P2) is given by

$$\theta^* = \arg \max \{ \text{SNR}_2(f(n)), \text{SNR}_2(\theta_l) \}, \quad (20)$$

where if  $\Gamma \neq 0$ , then  $f(n)$  exists with

$$n = \begin{cases} 2 \lceil \frac{\sqrt{(y_1 - y_0)^2 + (2x_1 - \frac{y_1 - y_0}{\tan \theta_l})^2} - \frac{y_1 - y_0}{\sin \theta_l}}{\lambda} \rceil, & 0 < \Gamma, \\ 2 \lceil \frac{\sqrt{(y_1 - y_0)^2 + (2x_1 - \frac{y_1 - y_0}{\tan \theta_r})^2} - \frac{y_1 - y_0}{\sin \theta_r}}{\lambda} \rceil + 1, & \Gamma < 0. \end{cases} \quad (21)$$

The accuracy of the above proposed closed-form solution will be validated in simulations.

## V. GROUP RELATIVE POLICY OPTIMIZATION

Due to the complicated structure of Problem (P1), we customize the use of an advanced DRL algorithm, GRPO [40], recently proposed by the research team at DEEPSEEK, offering an efficient approach to tackling this complex problem.

### A. MDP Definition

As a foundation of DRL, we define Markov Decision Process (MDP) *state*, *action*, and *reward* as follows:

- *MDP state*  $\mathbf{s}$  is defined by  $(\mathcal{L}, \mathcal{X}, \{\mathbf{h}_k(\boldsymbol{\theta})\})$ . Note that the state will transition based on the action taken.
- *MDP action*  $\mathbf{a}$  is defined by  $(\boldsymbol{\theta}, \{\boldsymbol{\omega}_k\})$ . The action is the optimization variables for Problem (P1).
- *MDP reward*  $r$  is defined by

$$r = \sum_{k=1}^K \log_2 \left( 1 + \frac{|\mathbf{h}_k^H(\boldsymbol{\theta}) \boldsymbol{\omega}_k|^2}{\sum_{k' \neq k} |\mathbf{h}_{k'}^H(\boldsymbol{\theta}) \boldsymbol{\omega}_k|^2 + \sigma^2} \right), \quad (22)$$

if constraints (1a)-(1c) are satisfied. Otherwise, the *MDP reward*  $r$  will be a large negative number. The reward is the optimization objective for Problem (P1).

- *MDP observation*  $\mathbf{o}$  corresponds to the successor state following an action.

Based on the above MDP definition, the optimal action made from states leads to an optimized solution to Problem (P1).

### B. Proposed GRPO Solution

DRL employs the MDP framework, where agents learn optimal policies by maximizing cumulative rewards through state-action value functions approximated by neural networks. PPO stands as a prominent policy gradient algorithm in DRL that addresses the instability of traditional policy optimization methods through a constrained update mechanism. Introduced by OpenAI in 2017 [42], PPO's core innovation lies in its clipped surrogate objective function, which restricts policy changes by limiting the ratio between new and old policy probabilities to a predefined interval, effectively creating a trust region that prevents destructively large updates.

GRPO is a nontrivial variant of PPO [42]. Unlike PPO, GRPO offers the distinct benefit of reduced resource demands during training, as noted in [40]. Specifically, GRPO replaces the resource-intensive critic network of PPO with a set of trajectories, collectively termed a "group". The advantage function for a policy is therefore calculated using relative advantage functions within the group. This advantage is then used to update the actor (policy) network through stochastic gradient descent. This framework is shown in Fig. 7.

According to [40], GRPO aims to optimize the parameters  $w$  by maximizing the objective  $\mathcal{J}_{\text{GRPO}}(w)$  in (23). As its key innovation, the advantage function in (23) is computed through group relative advantage estimation:

$$\hat{A}_g = \frac{r_g - \text{mean}(\{r_1, \dots, r_G\})}{\text{std}(\{r_1, \dots, r_G\})}, \quad (24)$$

where the operations  $\text{mean}\{\cdot\}$  and  $\text{std}\{\cdot\}$  denote the mean and standard deviation of set  $\{\cdot\}$ , respectively.

We define the trajectory-wise reward  $r_g$ ,  $g \in [G]$  by the reward at the last observation  $\mathbf{o}_g$ . This is particularly fitting for our problem, since the solution of Problem (P2) is given at the last observation. According to [40], the clip function in (23) is used for limiting drastic policy updates:

$$\text{clip} \left( \frac{\pi_w(\mathbf{o}_g, t | \mathbf{a}, \mathbf{o}_{g, < t})}{\pi_{w_{\text{old}}}(\mathbf{o}_g, t | \mathbf{a}, \mathbf{o}_{g, < t})}, 1 - c, 1 + c \right)$$

$$\mathcal{J}_{\text{GRPO}}(w) = \mathbb{E} \left[ \frac{1}{G} \sum_{g=1}^G \frac{1}{O_g} \sum_{t=1}^{O_g} \left\{ \min \left( \frac{\pi_w(\mathbf{o}_{g,t} | \mathbf{a}, \mathbf{o}_{g,<t})}{\pi_{w_{\text{old}}}(\mathbf{o}_{g,t} | \mathbf{a}, \mathbf{o}_{g,<t})}, \text{clip} \left( \frac{\pi_w(\mathbf{o}_{g,t} | \mathbf{a}, \mathbf{o}_{g,<t})}{\pi_{w_{\text{old}}}(\mathbf{o}_{g,t} | \mathbf{a}, \mathbf{o}_{g,<t})}, 1 - c, 1 + c \right) \right\} \hat{A}_g - \eta \mathbb{D}_{\text{KL}}[\pi_w \| \pi_{\text{ref}}] \right\} \right] \quad (23)$$

---

**Algorithm 2:** Algorithm for GRPO Training

---

**Input:**  $\mathcal{L}, \mathcal{X}, T$  and other hyperparameters  
1 Generate  $\pi_{\text{ref}}$  by training PPO [42] for  $T$  steps  
2 **for**  $\text{Iteration} = 1, \dots, I$  **do**  
3     Update the old policy  $\pi_{w_{\text{old}}} \leftarrow \pi_w$   
4     Sample  $G$  outputs  $\{\mathbf{o}_g\}_{g=1}^G \sim \pi_{w_{\text{old}}}(\cdot | \mathbf{a})$  for a randomly selected action  $\mathbf{a}$   
5     Compute rewards  $\{r_g\}_{g=1}^G$  for each  $\mathbf{o}_g, g \in [G]$   
6     Compute advantage function  $\hat{A}_g$  using (24)  
7     **for**  $\text{GRPO iteration} = 1, \dots, \mu$  **do**  
8         Update the policy  $\pi_w$  through maximizing (23)  
9     **end**  
10 **end**  
**Output:**  $\pi_w$

---

$$= \max \left( \min \left( \frac{\pi_w(\mathbf{o}_{g,t} | \mathbf{a}, \mathbf{o}_{g,<t})}{\pi_{w_{\text{old}}}(\mathbf{o}_{g,t} | \mathbf{a}, \mathbf{o}_{g,<t})}, 1 + c \right), 1 - c \right). \quad (25)$$

The Kullback-Leibler (KL) divergence in (23) is utilized to regulate the difference between the updated policy and the reference policy  $\pi_{\text{ref}}$ , with its importance controlled by KL penalty  $\eta \geq 0$ . According to [40], KL divergence can be approximately calculated by

$$\mathbb{D}_{\text{KL}}[\pi_w \| \pi_{\text{ref}}] \approx \frac{\pi_{\text{ref}}(\mathbf{o}_{g,t} | \mathbf{a}, \mathbf{o}_{g,<t})}{\pi_w(\mathbf{o}_{g,t} | \mathbf{a}, \mathbf{o}_{g,<t})} - \log \frac{\pi_{\text{ref}}(\mathbf{o}_{g,t} | \mathbf{a}, \mathbf{o}_{g,<t})}{\pi_w(\mathbf{o}_{g,t} | \mathbf{a}, \mathbf{o}_{g,<t})} - 1. \quad (26)$$

Finally, the used algorithm for GRPO training is summarized in Algorithm 2, where we invoke the PPO algorithm for  $T$  steps for obtaining a reference policy. Note that the steps of  $T$  is small, and the PPO algorithm does not need to converge.

### C. Computational Complexity

To compare the complexity of GRPO and PPO, we analyze the computational complexity of the only actor network (GRPO) and the actor and critic networks (PPO). Suppose that both actor and critic networks have  $L_{\text{hidden}}$  layers and each layer has  $L$  neurons. According to [41], the computational complexity for the actor network is on the order of  $\mathcal{O}(d_s L + \underbrace{L^2 + \dots + L^2}_{L_{\text{hidden}}} + L d_a) = \mathcal{O}(L(d_s + d_a + L L_{\text{hidden}}))$ , and critic network is on the order of  $\mathcal{O}(d_s L + \underbrace{L^2 + \dots + L^2}_{L_{\text{hidden}}} + L) =$

$\mathcal{O}(L(d_s + 1 + L L_{\text{hidden}}))$ , where  $d_s$  denotes the state dimension and is equal to  $2K + 2 + 2M$  and  $d_a$  denotes the action dimension and is equal to  $N + 2KN$ . Therefore, PPO and GRPO have  $\mathcal{O}(L(2d_s + d_a + 1 + 2L L_{\text{hidden}}))$  and  $\mathcal{O}(L(d_s + d_a + L L_{\text{hidden}}))$  computational complexity for neural networks, respectively. It can be seen that GRPO reduces

TABLE III: CONFIGURATION & LEARNING PARAMETERS

Policy (Actor) Network				
Component	Type	Input/Output	Activation	
Input Layer	Linear	Input	ReLU	
Hidden Layer	Linear	Size $\times$ 256	ReLU	
Output Layer	Linear	256 $\times$ Output	-	
Critic Network				
Component	Type	Input/Output	Activation	
Input Layer	Linear	Input $\times$ 256	ReLU	
Hidden Layer	Linear	256 $\times$ 256	ReLU	
Output Layer	Linear	256 $\times$ Output	-	
Learning Parameters				
Learning Rate	KL Penalty	Clipping Threshold	Batch Size	
$9.46 \times 10^{-4}$	0.0001	0.1	64	

the computational complexity of neural networks by approximately half compared to PPO.

## VI. SIMULATIONS

### A. Simulation Setup

In simulations, the AWGN variance is  $\sigma^2 = 10^{-12}$ , and the maximal transmit power is  $P_{\text{max}} = 1$  W. The relative permittivity of walls is  $\epsilon = 5.24$ , which is that of concrete [27]. The antenna gains at Tx  $G_t$  and Rx  $G_r$  are both equal to 1. The neural network configurations in PPO and GRPO (only with policy network) are listed in Table III, where we adopt moderate scale actor and critic networks for our problem. Baseline algorithms for comparison with GRPO are below.

**PPO Init.** (PPO proposed in [42] training  $T = 25$  K steps as our GRPO reference policy): The baseline consists of training PPO [42] for 25 K steps, a process that takes roughly 3 minutes on our computer. Our GRPO method uses this trained policy as its reference policy for initialization.

**PPO** (PPO proposed in [42]): This baseline trains PPO [42] until 3 million steps. It is known that PPO has a superior performance. This baseline is to test how much the performance gain can be obtained from PPO in [42].

**A2C** (A2C applied in [35]): This baseline trains A2C until 3 million steps. A2C algorithm combines policy learning with value estimation to reduce variance while maintaining direct policy optimization. Differently, A2C lacks PPO's trust region constraints, making it simpler but less stable during training. A2C shows its success in FAS-ISAC [35].

**WMMSE-FP** (Fixed fluid antenna position, WMMSE beamforming and power allocation [43]): This baseline fixes the fluid antenna position. Meanwhile, WMMSE [43] is applied to optimize beamforming and transmit power. We randomly sample 200 antenna positions for averaging its performance, since it takes a fixed antenna position and is susceptible to unsatisfactory positions.

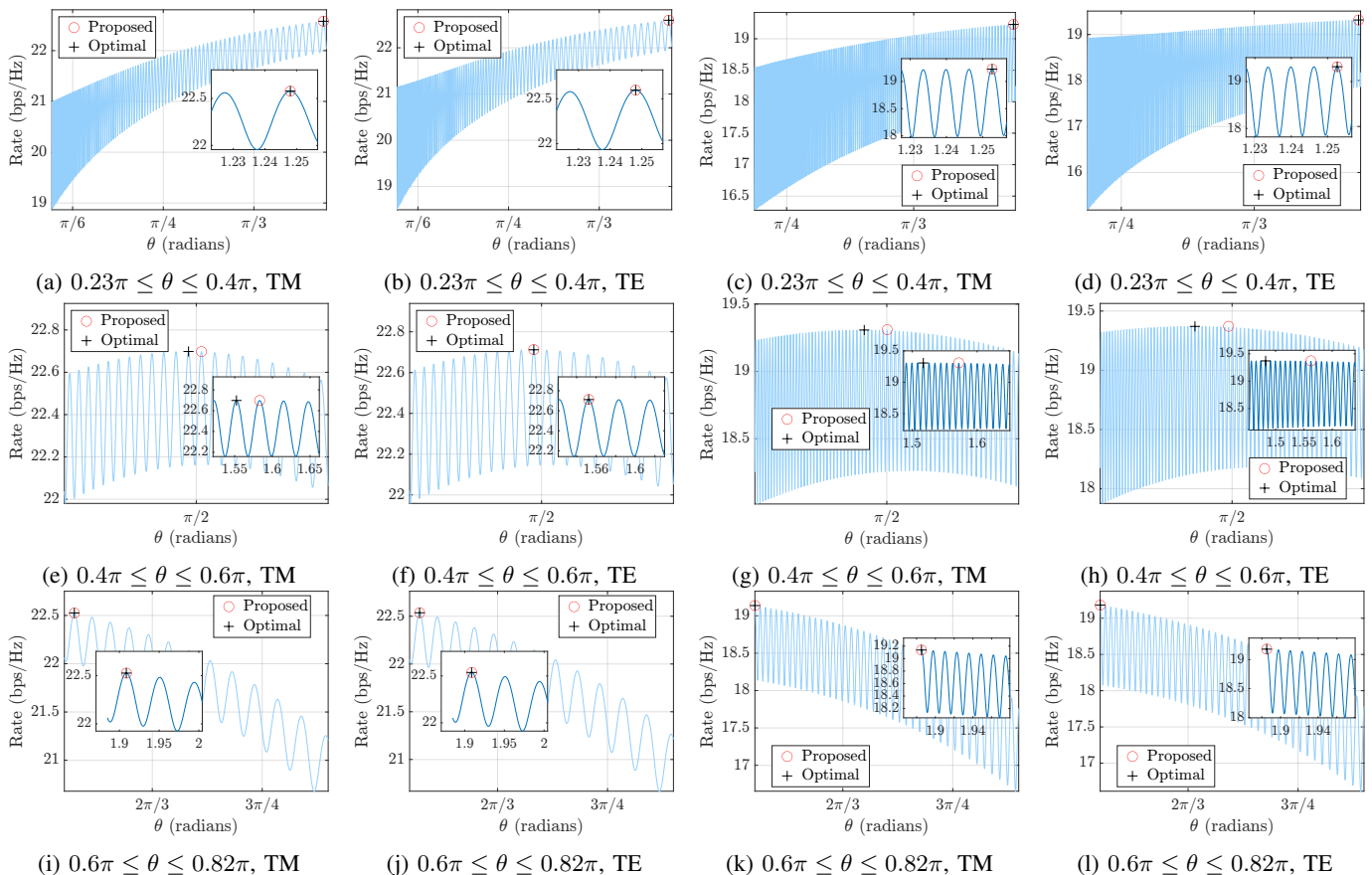


Fig. 8:  $G_t = G_r = 1$ ,  $\sigma^2 = -90$  dBm,  $f = 5$  GHz,  $\epsilon = 5.24$  m, where  $x_1 = y_1 = 4$  m,  $y_0 = 2$  m for (8a),(8b),(8e),(8f),(8i),(8j), and  $x_1 = y_1 = 4$  m,  $y_0 = 0.5$  m for (8c),(8d),(8g),(8h),(8k),(8l).

**WMMSE-GS** (Fluid antenna position with grid search (GS), beamforming, and power allocation with WMMSE [43]): Search fluid antenna positions via grid. The grid is given by  $0, \Delta, 2\Delta, \dots, 25\Delta$ , where  $\Delta = \lambda/2 = 0.03$  m is the minimal distance between two adjacent antennas. This baseline exhaustively evaluates all  $\binom{26}{N}$  possible antenna positions to find the optimal combination. For each combination, beamforming and power allocation are optimized using WMMSE algorithm [43]. This baseline aims to examine the GRPO advantage over the state-of-the-art numerical optimization method.

### B. Performance Evaluation

In Fig. 8, we examine the performance of the proposed closed-form solution, where Fig. 8 shows different Tx and Rx placement. Fig. 8 shows that the proposed closed-form solution is exactly the same as the globally optimal solution by exhaustive search for  $0.23\pi \leq \theta \leq 0.4\pi$  and  $0.6\pi \leq \theta \leq 0.82\pi$ . While, there is a slight difference between the proposed closed-form solution and the globally optimal solution by exhaustive search for  $0.4\pi \leq \theta \leq 0.6\pi$ . This can be interpreted as follows: The behavior of the rate function in  $0.23\pi \leq \theta \leq 0.4\pi$  and  $0.6\pi \leq \theta \leq 0.82\pi$  is primarily determined by a pronounced increasing or decreasing trend. Therefore, the proposed closed-form solution, that is, the local maximizer near the boundary, is globally optimal. In contrast, within  $0.4\pi \leq \theta \leq 0.6\pi$ , the rate function exhibits a non-monotonic

TABLE IV: Performance comparison of PPO Init. and the proposed closed-form in Section IV, where the layout is rectangular with corner points  $\{(0, 0), (0, 5), (5, 5), (5, 0)\}$  (Unit: m). Tx fluid antenna position is  $y = 0.5$  m,  $0.6\pi \leq \theta \leq 0.82\pi$  (Rx position 1), and  $0.23\pi \leq \theta \leq 0.3\pi$  (Rx position 2).

Frequency, Rx Location	Method	Rate (bps/Hz)	Solution $\theta^*$
5GHz, RX Position 1 (1.5m, 1.5m)	PPO Init.	25.4154	0.6084 $\pi$
	Closed-Form	<b>25.4155</b>	0.6084 $\pi$
60GHz, RX Position 1 (1.5m, 1.5m)	PPO Init.	18.8406	0.6010 $\pi$
	Closed-Form	<b>18.8406</b>	0.6010 $\pi$
5GHz, RX Position 2 (4.25m, 3m)	PPO Init.	19.9056	0.2967 $\pi$
	Closed-Form	<b>20.9301</b>	0.2998 $\pi$
60GHz, RX Position 2 (4.25m, 3m)	PPO Init.	14.4242	0.2967 $\pi$
	Closed-Form	<b>16.0837</b>	0.2998 $\pi$

behavior, increasing until  $\pi/2$  and then decreasing. Thus, the proposed closed-form solution, i.e., the local maximizer near to  $\pi/2$ , may not be globally optimal, which is validated in Fig. 8. As for  $0.4\pi \leq \theta \leq 0.6\pi$ , Fig. 8 shows that the proposed solution approaches the globally optimal solution, having a near-optimal performance.

In Table IV, we further examine the proposed closed-form solution in a practical layout and compare it with PPO init.

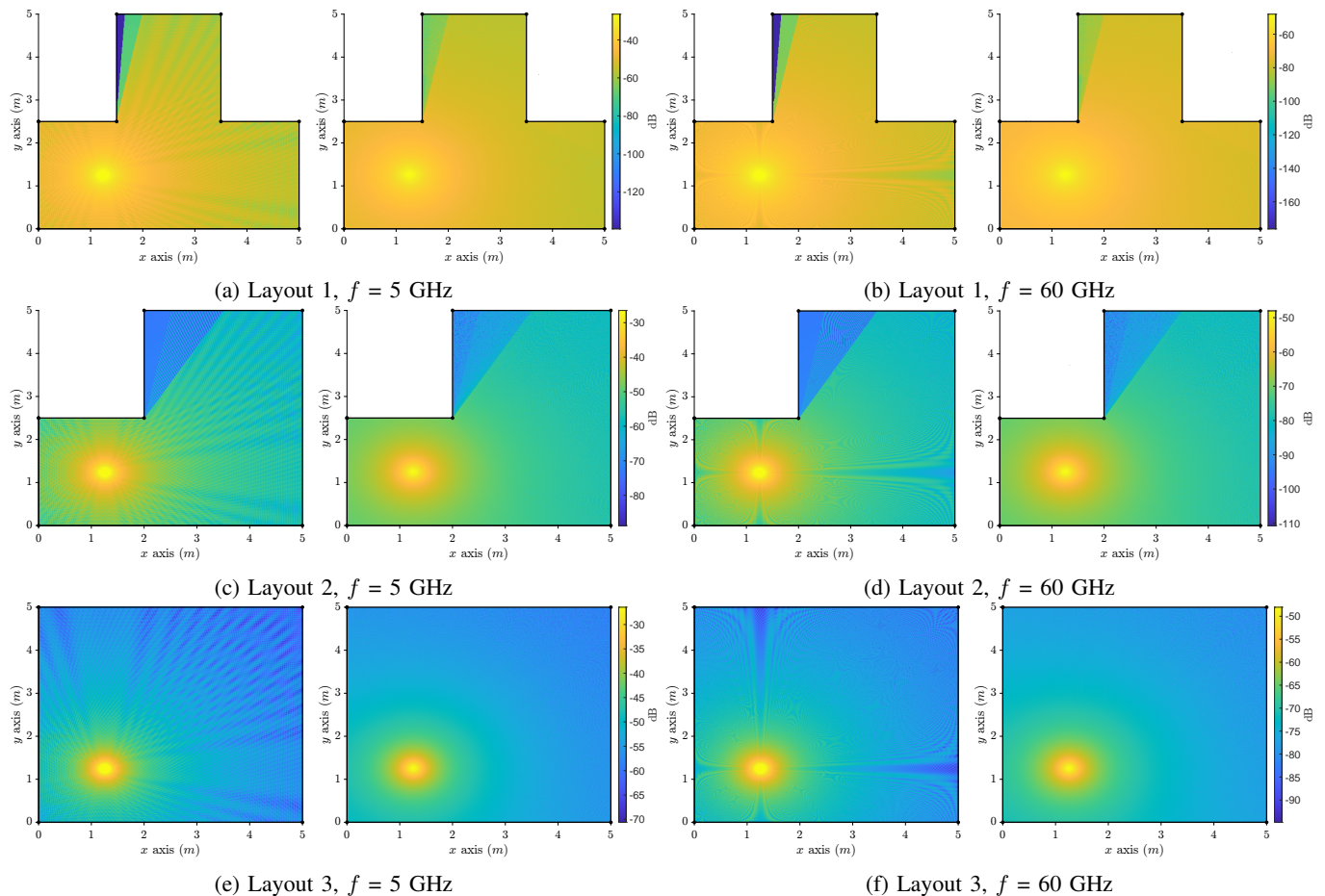


Fig. 9: Performance comparison of proposed channel model with Sionna, where for each layout, the left one is the PL heatmap proposed and the right one is the PL heatmap by Sionna [27].

TABLE V: PERFORMANCE COMPARISON OF PROPOSED CHANNEL MODEL WITH SIONNA [27].

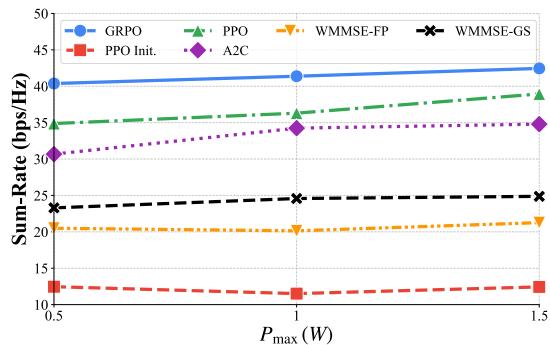
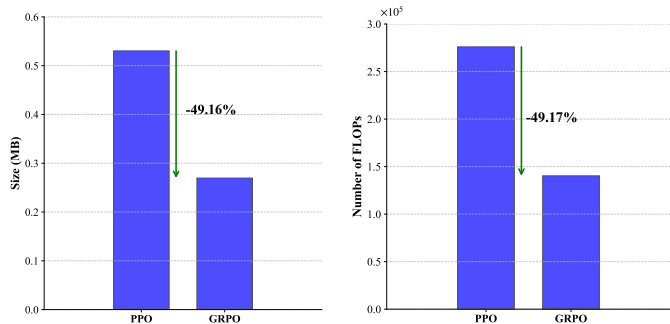
Layout, Frequency	MAE (dB)		RMSE (dB)		Average Rate (bps/Hz)	Average Rate (bps/Hz), Sionna		Times (s)	Times (s), Sionna	
	1 <sup>st</sup> &2 <sup>nd</sup>	Full	1 <sup>st</sup> &2 <sup>nd</sup>	Full	Ours	1 <sup>st</sup> &2 <sup>nd</sup>	Full	Ours	1 <sup>st</sup> &2 <sup>nd</sup>	Full
1, 5GHz	1.8234	1.8496	2.5542	2.5935	15.7479	16.0936	16.1032	679.8	2023.4	3609.8
1, 60GHz	1.9835	2.0092	2.7924	2.8251	10.7185	11.0554	11.0659	686.6	1858.4	3487.4
2, 5GHz	2.2681	2.2498	3.5297	3.3586	17.6271	17.8886	17.9231	575.5	1896.7	3547.0
2, 60GHz	2.3982	2.3610	3.7151	3.4513	11.8190	12.1181	12.1568	569.6	1855.1	3505.4
3, 5GHz	1.9391	1.9542	2.6944	2.7179	22.3751	22.6285	22.6379	483.1	1647.5	3294.2
3, 60GHz	2.1596	2.1737	3.0363	3.0576	15.0859	15.4552	15.4667	485.7	1646.3	3275.5

baseline. Table IV demonstrates that the proposed closed-form solution outperforms the PPO init. baseline, even after the latter's 25 K-steps training. This performance gap widens as the distance between the Tx and Rx increases. The reason for this is that NLoS rays reflected from other walls become progressively weaker compared to the two-rays, consisting of a wall reflection NLoS ray and the LoS ray, utilized by the proposed closed-form solution. Table IV shows that our physics-informed closed-form solution could outperform general-purpose algorithms.

In Fig. 9, we compare the radio maps generated by the proposed layout-specific RT model with those from Sionna with

full-order reflection [27], where  $G_t = G_r = 1$ ,  $\epsilon = 5.24$ , TM mode, and single antenna. Fig. 9 reveals a strong consensus in the spatial PL between our model and Sionna generations, except that our model exhibits more pronounced coloration in regions distant from Tx and near corners, whereas Sionna does not show this feature. This discrepancy arises from the fact that our model only accounts for first-order reflection, which cannot reach these specific regions, whereas Sionna's algorithm incorporates full-order reflection paths.

A detailed comparison of Fig. 9 is presented in Table V. The results indicate that our model achieves mean absolute error (MAE) and RMSE of approximately 2 dB and 3 dB

(a) GRPO v.s. baselines with different  $P_{\max}$ .

(b) Model size reduction.

(c) FLOPs reduction.

Fig. 10: Sum-rate, model size, and FLOPs comparison of GRPO with baselines.

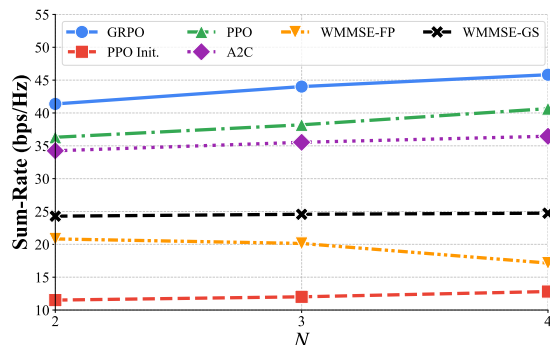
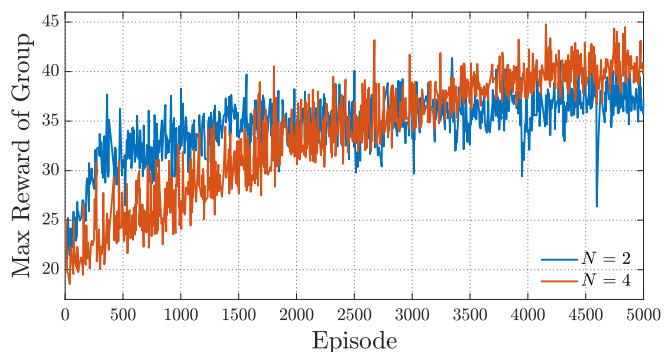
(a) GRPO v.s. baselines with different  $N$ .(b) GRPO training with  $N = 2$  and  $N = 4$ .

Fig. 11: Sum-rate comparison of GRPO with baselines.

for Sionna 1<sup>st</sup>&2<sup>nd</sup>- and full-order reflection models. Furthermore, the average rate over the radio map (calculated at a 1 cm<sup>2</sup> resolution) is comparable to Sionna 1<sup>st</sup>&2<sup>nd</sup>- and full-order reflection models. The negligible performance difference between Sionna 1<sup>st</sup>&2<sup>nd</sup>- and full-order models implies that the first and second-order reflections are dominant in these 3 scenarios. Most significantly, our model offers a substantial computational advantage, requiring only 1/3 and 1/6 of the time of Sionna second and full-order models, respectively.

In Fig. 10, we evaluate the performance of the proposed GRPO solution across different maximal transmit power. The simulation computer platform is with NVIDIA GeForce Laptop 4090 16G and INTEL Core i9-13600. We consider a rectangular layout with corner points  $\{(0, 0), (0, 5), (5, 5), (5, 0)\}$  (Unit: m). A two-antenna transmitter is located at  $(x_0, 0.5)$  m, where  $x_0 \in [3.5, 4.25]$  m, and two receivers are located at  $(1.25, 1.25)$  m and  $(4.25, 3.0)$  m, respectively. The frequency is 5 GHz. For GRPO, we take group size 50 and trajectory length 5. Specifically, Fig. 10a highlights the superior sum-rate achieved by GRPO compared to baselines listed above, exhibiting a significant improvement over the GRPO reference policy. This result highlights GRPO's capability to transform poorly-performing policies into ones that deliver superior performance.

Furthermore, Fig. 10a shows that as maximal transmit power increases, GRPO consistently outperforms all baselines, with a notable gain at a higher maximal transmit power. This implies

the effectiveness of GRPO in jointly optimizing the antenna positions, beamforming vectors, and transmit power allocation, especially when abundant transmission resources are available. Fig. 10b shows a 49.2% reduction in model size when using GRPO compared to PPO. Aligned with [40], this reduction shows that GRPO can achieve better performance with a more compact neural network model.

Fig. 10c demonstrates a significant reduction in FLOPs during training when using GRPO, primarily attributed to the elimination of the value model and optimized group-based sampling. Compared to traditional PPO, GRPO achieves a substantial reduction in computational overhead, reflecting its superior efficiency in resource utilization. This efficiency gain directly translates to lower training costs, making GRPO a more practical and scalable solution for large-scale model training, particularly in resource-constrained environments.

In Fig. 11, we evaluate the performance of the proposed GRPO solution across different number of transmit antennas. Unless specified otherwise, we use the same parameters and experiment environment as in Fig. 10. Here, we take group size 50, trajectory length 5, and  $P_{\max} = 1$  W. Fig. 11a shows that except WMMSE-FP, all algorithms attain their maximum sum-rate at 4 transmit antennas, since more transmit antennas can provide greater beamforming gain. The sum-rate of WMMSE-FP at 4 transmit antennas is not the highest, because WMMSE-FP employs a fixed antenna position with randomized experiments, preventing it from fully exploiting the beamforming

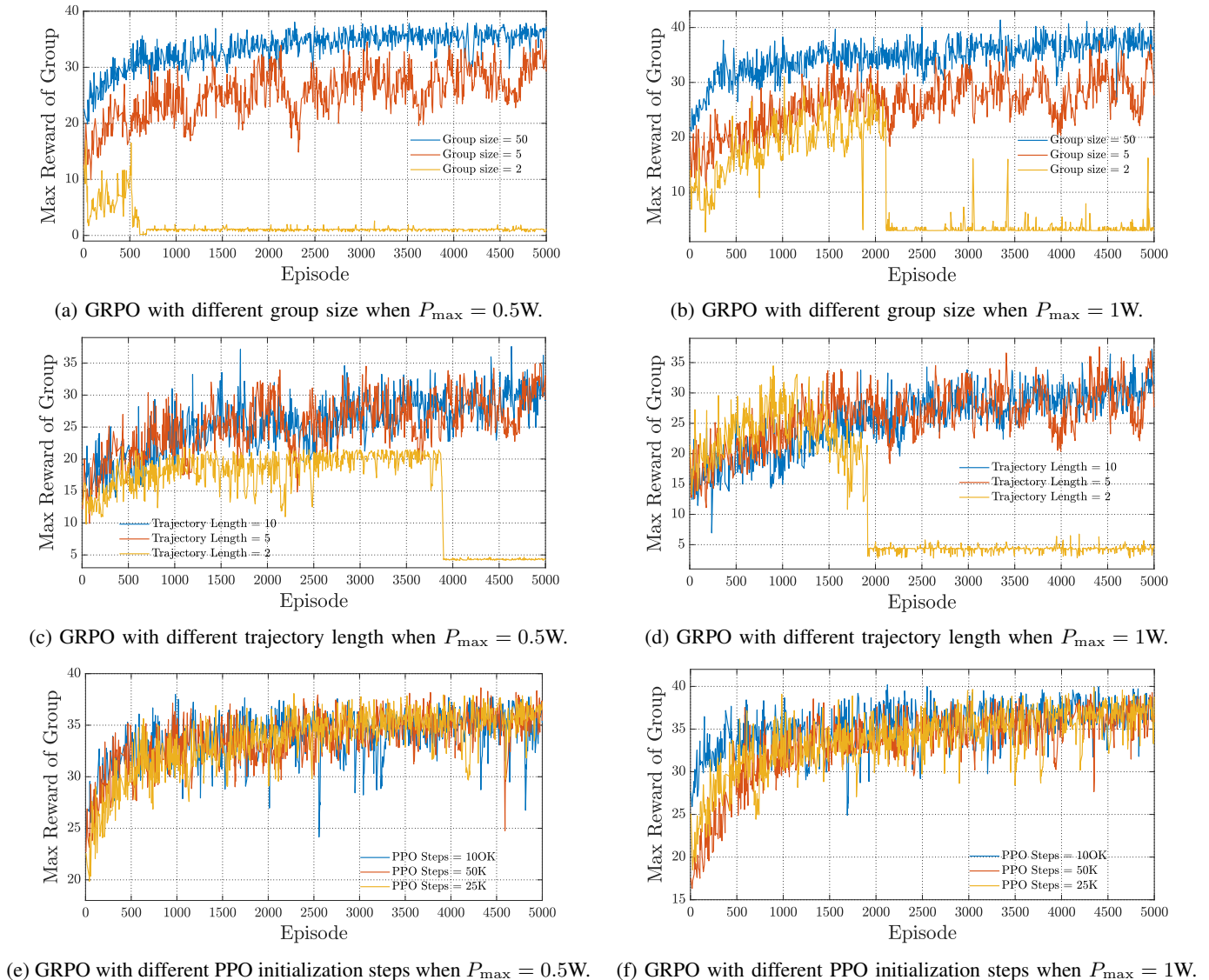


Fig. 12: Comparison of different group size, trajectory length, and PPO initialization steps for GRPO.

gain as the number of antennas grows. In contrast, WMMSE-GS can exploit the beamforming gain by searching with a larger number of antennas on the grid. In addition, Fig. 11b shows that the maximal reward of group with 4 transmit antennas eventually defeats the maximal reward of group with 2 transmit antennas after 5000 episodes. This outcome aligns with more beamforming gain at 4 transmit antennas.

In Fig. 12, we investigate how group size, trajectory length, and PPO initialization steps affect the performance of GRPO. Unless specified otherwise, we use the same parameters and experiment environment as in Fig. 10. The group size and trajectory length are critical for balancing the celebrated trade-off between exploration and exploitation. In particular, a larger group size and trajectory length encourages exploration, while a smaller group size and trajectory length encourage exploitation [40], since a reward is given at the last observation of a trajectory. Given trajectory length 5, Figs. 12a and 12b show that regarding group maximal reward, the group size 50 enjoys a moderate gain and less fluctuation compared with

group size 5, where the training with group size 50 costs approximately 25 hours while the training with group size 5 costs approximately 4 hours. This implies that increasing the group size could not lead to a significant enhancement but consuming a large amount of training time. Furthermore, Figs. 12a and 12b show that a small group size, i.e., group size 2, leads to a collapse, since it is easily trapped. Given group size 5, Figs. 12c and 12d show that regarding group maximal reward, trajectory length 10 has a similar performance to trajectory length 5. This implies that increasing the trajectory length may not lead to continuous performance enhancement. Figs. 12c and 12d show that a small trajectory length, i.e., trajectory length 2, leads to a collapse as well. Given group size 50 and trajectory length 5, Figs. 12c and 12d show that different PPO initialization steps lead to a similar performance. This shows that GRPO has an excellence optimization capability irregardless of PPO initialization steps. To summarize, the results in Fig. 12 highlight the importance of tailoring the group size and trajectory length to the environmental

complexity and computational constraints.

## VII. CONCLUSIONS

In this paper, we investigated how FAS can enhance indoor wireless communications by addressing critical challenges in channel modeling and system optimization/configuration. Specifically, our key contributions include the following: 1) developing a layout-specific ray-tracing model that achieves an 83.3% reduction in computational time compared to Sionna RT while only 3 dB RMSE loss, enabling real-time multipath tracking; 2) deriving a closed-form solution for the two-ray model that preserves near-optimal performance; and 3) proposing a GRPO optimization solution for jointly optimizing antenna positions, beamforming, and power allocation. Notably, our simulation result reveals that increasing the group size and trajectory length for GRPO does not yield prominent sum-rate improvement while consuming a large amount of training time, suggesting the importance of group size and trajectory length selection. Furthermore, the GRPO algorithm shows superior sum rate performance over the PPO, A2C, and WMMSE approaches while requiring 49.2 fewer FLOPs than PPO. In the future, our indicator function framework can be extended to incorporate second-order reflection by computing two reflection points.

### APPENDIX A

#### ANGLE-DEPENDENT DISTANCE DERIVATION EXAMPLE

Consider the room layout illustrated in Fig. 1 as an example. Since walls are either perpendicular to  $x$ -axis or  $y$ -axis, it can be easily observed from Fig. 1 that

$$D^{[1]}(\mathcal{L}, \mathcal{X}) = \begin{cases} x_0, & \text{Wall 1,} \\ y_1^c - y_0, & \text{Wall 2,} \\ x_5^c - x_0, & \text{Wall 5,} \\ y_0, & \text{Wall 6,} \end{cases} \quad (27a)$$

$$D^{[2]}(\mathcal{L}, \mathcal{X}) = \begin{cases} x_1, & \text{Wall 1,} \\ y_1^c - y_1, & \text{Wall 2,} \\ x_5^c - x_1, & \text{Wall 5,} \\ y_1, & \text{Wall 6,} \end{cases} \quad (27b)$$

$$D^{[3]}(\mathcal{L}, \mathcal{X}) = \begin{cases} y_1 - y_0, & \text{Wall 1,} \\ x_1 - x_0, & \text{Wall 2,} \\ y_1 - y_0, & \text{Wall 5,} \\ x_1 - x_0, & \text{Wall 6.} \end{cases} \quad (27c)$$

By means of substituting  $x_0 = x_1 - \frac{y_1 - y_0}{\tan \theta}$  into (27a)-(27c), we derive the angle-dependent distance functions  $D^{[1]}(\theta)$ ,  $D^{[2]}(\theta)$ , and  $D^{[3]}(\theta)$ . This ends the example.

### APPENDIX B

#### PROOF OF THEOREM 1

It can be seen that  $D^{[1]}(\theta) = x_1 - \frac{y_1 - y_0}{\tan \theta}$ ,  $D^{[2]}(\theta) = x_1$ , and  $D^{[3]}(\theta) = y_1 - y_0$ . Thus, we have

$$d_{\text{NLoS}} = d_1 + d_2 = \sqrt{(y_1 - y_0)^2 + \left(2x_1 - \frac{y_1 - y_0}{\tan \theta}\right)^2}, \quad (28)$$

$\Gamma(\theta)$  is given by (3) with

$$\alpha = \arctan\left(\frac{2x_1}{y_1 - y_0} - \frac{1}{\tan \theta}\right), \quad (29)$$

and  $d_{\text{LoS}}$  is given in (9). This leads to

$$h_2(\theta) = \frac{\sqrt{G_t G_r} \lambda}{4\pi} \times \left( \frac{e^{-j2\pi \frac{y_1 - y_0}{\lambda \sin \theta}}}{d_{\text{LoS}}} + \frac{\Gamma e^{-j2\pi \frac{\sqrt{(y_1 - y_0)^2 + (2x_1 - \frac{y_1 - y_0}{\tan \theta})^2}}{\lambda}}}{\sqrt{(y_1 - y_0)^2 + (2x_1 - \frac{y_1 - y_0}{\tan \theta})^2}} \right). \quad (30)$$

Since  $\text{SNR}_2(\theta) = \frac{|h_2(\theta)|^2}{\sigma^2}$ , we have

$$\text{SNR}_2(\theta) = \frac{G_t G_r \lambda^2}{\sigma^2 (4\pi)^2} \left( \left( \frac{\sin \theta \cos(2\pi \frac{y_1 - y_0}{\lambda \sin \theta})}{y_1 - y_0} + \frac{\Gamma \cos(2\pi \frac{\sqrt{(y_1 - y_0)^2 + (2x_1 - \frac{y_1 - y_0}{\tan \theta})^2}}{\lambda})}{\sqrt{(y_1 - y_0)^2 + (2x_1 - \frac{y_1 - y_0}{\tan \theta})^2}} \right)^2 + \left( \frac{\sin \theta \sin(2\pi \frac{y_1 - y_0}{\lambda \sin \theta})}{y_1 - y_0} + \frac{\Gamma \sin(2\pi \frac{\sqrt{(y_1 - y_0)^2 + (2x_1 - \frac{y_1 - y_0}{\tan \theta})^2}}{\lambda})}{\sqrt{(y_1 - y_0)^2 + (2x_1 - \frac{y_1 - y_0}{\tan \theta})^2}} \right)^2 \right). \quad (31)$$

By expanding (31) and applying the trigonometric identity  $\cos^2(\cdot) + \sin^2(\cdot) = 1$ , we can prove Theorem 1.

### APPENDIX C

#### PROOF OF PROPOSITION 1

First of all, note that we aim at finding  $\bar{\theta}$  satisfying

$$\cos \left( 2\pi \frac{\sqrt{(y_1 - y_0)^2 + (2x_1 - \frac{y_1 - y_0}{\tan \theta})^2} - \frac{y_1 - y_0}{\sin \theta}}{\lambda} \right) = \begin{cases} 1, & 0 < \Gamma, \\ -1, & \Gamma < 0. \end{cases} \quad (32)$$

By defining

$$n = \begin{cases} 2 \lfloor \frac{\sqrt{(y_1 - y_0)^2 + (2x_1 - \frac{y_1 - y_0}{\tan \theta_r})^2} - \frac{y_1 - y_0}{\sin \theta_r}}{\lambda} \rfloor, & 0 < \Gamma, \\ 2 \lfloor \frac{\sqrt{(y_1 - y_0)^2 + (2x_1 - \frac{y_1 - y_0}{\tan \theta_r})^2} - \frac{y_1 - y_0}{\sin \theta_r}}{\lambda} \rfloor - 1, & \Gamma < 0, \end{cases} \quad (33)$$

we seek to find  $\bar{\theta}$  that satisfies

$$\sqrt{(y_1 - y_0)^2 + (2x_1 - \frac{y_1 - y_0}{\tan \bar{\theta}})^2} - \frac{y_1 - y_0}{\sin \bar{\theta}} = \frac{\lambda n}{2}. \quad (34)$$

By squaring both sides and multiplying by  $\sin^2 \bar{\theta}$ , we have

$$(4x_1^2 - \frac{n^2 \lambda^2}{4}) \sin^2 \bar{\theta} - 4x_1(y_1 - y_0) \cos \bar{\theta} \sin \bar{\theta} = n \lambda (y_1 - y_0) \sin \bar{\theta}. \quad (35)$$

Dividing both sides by  $\sin \bar{\theta}$ , we obtain

$$(4x_1^2 - \frac{n^2 \lambda^2}{4}) \sin \bar{\theta} - 4x_1(y_1 - y_0) \cos \bar{\theta} = n \lambda (y_1 - y_0). \quad (36)$$

Because  $\cos \phi = \frac{4x_1^2 - \frac{n^2\lambda^2}{4}}{\sqrt{(4x_1^2 - \frac{n^2\lambda^2}{4})^2 + (4x_1(y_1 - y_0))^2}}$  and  $\sin \phi = \frac{-4x_1(y_1 - y_0)}{\sqrt{(4x_1^2 - \frac{n^2\lambda^2}{4})^2 + (4x_1(y_1 - y_0))^2}}$  with  $\phi = \arctan\left(\frac{-4x_1(y_1 - y_0)}{4x_1^2 - \frac{n^2\lambda^2}{4}}\right)$ , we can re-write (36) into

$$\sqrt{\left(4x_1^2 - \frac{n^2\lambda^2}{4}\right)^2 + (4x_1(y_1 - y_0))^2} \sin(\bar{\theta} + \phi) = n\lambda(y_1 - y_0). \quad (37)$$

Finally, we invoke the arctan function to derive  $\bar{\theta}$  from (37) and let  $f(n) = \bar{\theta}$ . This completes the proof.

## REFERENCES

- [1] F. Tariq *et al.*, "A speculative study on 6G," *IEEE Wireless Commun.*, vol. 27, no. 4, pp. 118–125, Aug. 2020.
- [2] S. Dang, O. Amin, B. Shihada, and M.-S. Alouini, "What should 6G be?" *Nature Elect.*, vol. 3, no. 1, pp. 20–29, Jan. 2020.
- [3] R. Zhang *et al.*, "Integrated sensing and communication with massive MIMO: a unified tensor approach for channel and target parameter estimation," *IEEE Trans. Wireless Commun.*, vol. 23, no. 8, pp. 8571–8587, Aug. 2024.
- [4] G. J. Foschini, and M. Gans, "On limits of wireless communications in a fading environment when using multiple antennas," *Wireless Pers. Commun.*, vol. 6, pp. 311–335, Mar. 1998.
- [5] K. K. Wong, A. Shojaefard, K.-F. Tong, and Y. Zhang, "Fluid antenna systems," *IEEE Trans. Wireless Commun.*, vol. 20, no. 3, pp. 1950–1962, Mar. 2021.
- [6] K. K. Wong, W. K. New, X. Hao, K. F. Tong, and C. B. Chae, "Fluid antenna system—Part I: Preliminaries," *IEEE Commun. Lett.*, vol. 27, no. 8, pp. 1919–1923, Aug. 2023.
- [7] W. K. New *et al.*, "A tutorial on fluid antenna system for 6G networks: Encompassing communication theory, optimization methods and hardware designs," *IEEE Commun. Surv. & Tut.*, doi:10.1109/COMST.2024.3498855, 2024.
- [8] W.-J. Lu *et al.*, "Fluid antennas: Reshaping intrinsic properties for flexible radiation characteristics in intelligent wireless networks," accepted in *IEEE Commun. Mag.*, arXiv:2501.02911, 2025.
- [9] Y. Shen *et al.*, "Design and implementation of mmWave surface wave enabled fluid antennas and experimental results for fluid antenna multiple access," *arXiv preprint*, arXiv:2405.09663, May 2024.
- [10] R. Wang *et al.*, "Electromagnetically reconfigurable fluid antenna system for wireless communications: Design, modeling, algorithm, fabrication, and experiment," *arXiv preprint*, arXiv:2502.19643v2, 2025.
- [11] J. Zhang *et al.*, "A novel pixel-based reconfigurable antenna applied in fluid antenna systems with high switching speed," *IEEE Open J. Antennas & Propag.*, vol. 6, no. 1, pp. 212–228, Feb. 2025.
- [12] B. Liu, K. F. Tong, K. K. Wong, C.-B. Chae, and H. Wong, "Be water, my antennas: Riding on radio wave fluctuation in nature for spatial multiplexing using programmable meta-fluid antenna," *arXiv preprint*, arXiv:2502.04693, 2025.
- [13] K. K. Wong and K. F. Tong, "Fluid antenna multiple access," *IEEE Trans. Wireless Commun.*, vol. 21, no. 7, pp. 4801–4815, Jul. 2022.
- [14] K. K. Wong, A. Shojaefard, K.-F. Tong, and Y. Zhang, "Performance limits of fluid antenna systems," *IEEE Commun. Lett.*, vol. 24, no. 11, pp. 2469–2472, Nov. 2020.
- [15] Q. Zhang *et al.*, "An efficient sum-rate maximization algorithm for fluid antenna-assisted ISAC system," *IEEE Commun. Lett.*, vol. 29, no. 1, pp. 200–204, Jan. 2025.
- [16] M. Khammassi, A. Kammoun and M.-S. Alouini, "A new analytical approximation of the fluid antenna system channel," *IEEE Trans. Wireless Commun.*, vol. 22, no. 12, pp. 8843–8858, Dec. 2023.
- [17] J. D. Vega-Sánchez, L. Urquiza-Aguiar, M. C. P. Paredes, and D. P. M. Osorio, "A simple method for the performance analysis of fluid antenna systems under correlated Nakagami- $m$  fading," *IEEE Wireless Commun. Lett.*, vol. 13, no. 2, pp. 377–381, Feb. 2024.
- [18] Ericsson (2023) Indoor and outdoor mobile traffic. [Online]. Available: <https://www.ericsson.com/en/reports-and-papers/mobility-report/articles/indoor-outdoor>
- [19] J. Zhang *et al.*, "Fundamental wireless performance of a building," *IEEE Wireless Commun.*, vol. 29, no. 1, pp. 186–193, Feb. 2022.
- [20] M. K. Müller, M. Tarantetz, and M. Rupp, "Analyzing wireless indoor communications by blockage models," *IEEE Access*, vol. 5, pp. 2172–2186, 2016.
- [21] J. Zhang, A. A. Glazunov, and J. Zhang, "Wireless performance evaluation of building layouts: Closed-form computation of figures of merit," *IEEE Trans. Commun.*, vol. 69, no. 7, pp. 4890–4906, Jul. 2021.
- [22] F. Fuschini, E. M. Vitucci, M. Barbiroli, G. Falciasecca, and V. Degli-Esposti, "Ray tracing propagation modeling for future small-cell and indoor applications: A review of current techniques," *Radio Science*, vol. 50, no. 6, pp. 469–485, Jun. 2015.
- [23] Y. Zhang *et al.*, "How friendly are building materials as reflectors to indoor LOS MIMO communications?" *IEEE Int. Things J.*, vol. 7, no. 9, pp. 9116–9127, Sept. 2020.
- [24] Y. Zhang, J. Zhang, X. Chu, and J. Zhang, "Wireless friendliness evaluation and optimization for sandwich building materials as reflectors," *IEEE Trans. Antennas & Propag.*, vol. 72, no. 3, pp. 2697–2711, Mar. 2024.
- [25] Y. Chen, Y. Li, C. Han, Z. Yu, and G. Wang, "Channel measurement and ray-tracing-statistical hybrid modeling for low-terahertz indoor communications," *IEEE Trans. Wireless Commun.*, vol. 20, no. 12, pp. 8163–8176, Dec. 2021.
- [26] O. Kanhere, H. Poddar, and T. S. Rappaport, "Calibration of NYUray for ray tracing using 28, 73, and 142 ghz channel measurements conducted in indoor, outdoor, and factory scenarios," *IEEE Trans. Antennas & Propag.*, vol. 73, no. 1, pp. 405–420, Jan. 2025.
- [27] J. Hoydis *et al.*, "Sionna: An open-source library for next-generation physical layer research," *arXiv preprint*, arXiv:2203.11854v2, Mar. 2023.
- [28] W. K. New, K. K. Wong, H. Xu, K. F. Tong, and C.-B. Chae, "An information-theoretic characterization of MIMO-FAS: Optimization, diversity-multiplexing tradeoff and  $q$ -outage capacity," *IEEE Trans. Wireless Commun.*, vol. 23, no. 6, pp. 5541–5556, Jun. 2024.
- [29] W. Mei, X. Wei, B. Ning, Z. Chen, and R. Zhang, "Movable-antenna position optimization: A graph-based approach," *IEEE Wireless Commun. Lett.*, vol. 13, no. 7, pp. 1853–1857, Jul. 2024.
- [30] J. Yao *et al.*, "A framework of FAS-RIS systems: Performance analysis and throughput optimization," *IEEE Trans. Wireless Commun.*, pp. 1–1, 2025.
- [31] Z. Cheng *et al.*, "Sum-rate maximization for fluid antenna enabled multiuser communications," *IEEE Commun. Lett.*, vol. 28, no. 5, pp. 1206–1210, May 2024.
- [32] H. Qin *et al.*, "Antenna positioning and beamforming design for fluid antenna-assisted multi-user downlink communications," *IEEE Wireless Commun. Lett.*, vol. 13, no. 4, pp. 1073–1077, Apr. 2024.
- [33] T. Hao *et al.*, "Fluid-antenna enhanced ISAC: Joint antenna positioning and dual-functional beamforming design under perfect and imperfect CSI," *IEEE Trans. Veh. Technol.*, pp. 1–16, 2025.
- [34] Y. Ye *et al.*, "SCNR maximization for MIMO ISAC assisted by fluid antenna system," *IEEE Trans. Veh. Technol.*, vol. 74, no. 8, pp. 13272–13277, Aug. 2025.
- [35] C. Wang *et al.*, "Fluid antenna system liberating multiuser MIMO for ISAC via deep reinforcement learning," *IEEE Trans. Wireless Commun.*, vol. 23, no. 9, pp. 10879–10894, Sept. 2024.
- [36] P. Sharafi, L. H. Teh, and M. N. S. Hadi, "Conceptual design optimization of rectilinear building frames: A knapsack problem approach," *Engineering Optimization*, vol. 47, no. 10, pp. 1303–1323, 2015.
- [37] F. Rostami Ghadi, K.-K. Wong, F. Javier López-Martínez, C.-B. Chae, K.-F. Tong, and Y. Zhang, "A Gaussian copula approach to the performance analysis of fluid antenna systems," *IEEE Trans. Wireless Commun.*, vol. 23, no. 11, pp. 17573–17585, Nov. 2024.
- [38] P. Ramírez-Espinosa, D. Morales-Jimenez, and K.-K. Wong, "A new spatial block-correlation model for fluid antenna systems," *IEEE Trans. Wireless Commun.*, vol. 23, no. 11, pp. 15829–15843, Nov. 2024.
- [39] F. Fuschini, E. M. Vitucci, M. Barbiroli, G. Falciasecca, and V. Degli-Esposti, "Ray tracing propagation modeling for future small-cell and indoor applications: A review of current techniques," *Radio Science*, vol. 50, no. 6, pp. 469–485, 2015.
- [40] Z. Shao *et al.*, "Deepseekmath: Pushing the limits of mathematical reasoning in open language models," 2024. [Online]. Available: <https://arxiv.org/abs/2402.03300>.
- [41] J. S. Judd, "Neural network design and the complexity of learning," MIT Press, vol. 2, 1990.
- [42] J. Schulman, F. Wolski, P. Dhariwal, A. Radford, and O. Klimov, "Proximal policy optimization algorithms," 2017. [Online]. Available: <https://arxiv.org/abs/1707.06347>.
- [43] Q. Shi, M. Razaviyayn, Z.-Q. Luo, and C. He, "An iteratively weighted MMSE approach to distributed sum-utility maximization for a MIMO interfering broadcast channel," *IEEE Trans. Signal Process.*, vol. 59, no. 9, pp. 4331–4340, Sept. 2011.